Mon. Not. R. Astron. Soc. **357,** 1113–1133 (2005) doi:10.1111/j.1365-2966.2005.08715.x

Dynamical modelling of stars and gas in NGC 2974: determination of mass-to-light ratio, inclination and orbital structure using the Schwarzschild method

Davor Krajnović,[1]★ Michele Cappellari,[1] Eric Emsellem,[2] Richard M. McDermid[1] and P. Tim de Zeeuw[1]

[1]*Sterrewacht Leiden, Postbus 9513, 2300 RA Leiden, the Netherlands*
[2]*Centre de Recherche Astronomique de Lyon, 9 Avenue Charles André, 69230 Saint-Genis-Laval, France*

Accepted 2004 December 2. Received 2004 November 24; in original form 2004 October 7

ABSTRACT

We study the large-scale stellar and gaseous kinematics of the E4 galaxy NGC 2974, based on panoramic integral-field data obtained with SAURON. We quantify the velocity maps with Fourier methods (kinemetry), and show that the large-scale kinematics is largely consistent with axisymmetry. We construct general axisymmetric dynamical models for the stellar motions using the Schwarzschild orbit-superposition method, and compare the inferred inclination and mass-to-light ratio with the values obtained by modelling the gas kinematics. Both approaches give consistent results. However, we find that the stellar models provide fairly weak constraints on the inclination. The intrinsic orbital distribution of NGC 2974, which we infer from our model, is characterized by a large-scale stellar component of high angular momentum. We create semi-analytical test models, resembling NGC 2974, to study the ability of the Schwarzschild modelling technique to recover the given input parameters (mass-to-light ratio and inclination) and the distribution function. We also test the influence of a limited spatial coverage on the recovery of the distribution function (i.e. the orbital structure). We find that the models can accurately recover the input mass-to-light ratio, but we confirm that even with perfect input kinematics the inclination is only marginally constrained. This suggests a possible degeneracy in the determination of the inclination, but further investigations are needed to clarify this issue. For a given potential, we find that the analytical distribution function of our test model is well recovered by the three-integral model within the spatial region constrained by integral-field kinematics.

Key words: galaxies: elliptical and lenticular, cD – galaxies: individual: NGC 2974 – galaxies: kinematics and dynamics – galaxies: structure.

1 INTRODUCTION

The internal dynamical structure of galaxies retains evidence of their evolution. However, the internal dynamics can only be interpreted through a combination of observational and theoretical efforts. From a theoretical point of view, one wants to know how the stars are distributed in space and what velocities they have. From an observational point of view, one wants to determine the intrinsic structure of the observed galaxies. The goals of both approaches are equivalent, and consist of the recovery of the phase-space density, or distribution function (DF) of galaxies, which uniquely specifies their properties. An insight into the DF is possible by the construction of dynamical models that are constrained by observations. There are several modelling methods established in the literature, of which the Schwarzschild orbit-superposition method is perhaps the most elegant (Schwarzschild 1979, 1982). In the past few years it has been applied successfully to a number of galaxies (van der Marel et al. 1998; Cretton & van den Bosch 1999; Cappellari et al. 2002, hereafter C02; Gebhardt et al. 2003); however, recent observational advances in spectroscopy with integral-field units offer for the first time full two-dimensional (2D) constraints on these dynamical models (Verolme et al. 2002, hereafter V02; Copin, Cretton & Emsellem 2004).

In this paper we present a case study of the early-type galaxy NGC 2974. It is one of the few elliptical galaxies known to contain an extended disc of neutral hydrogen in regular rotation (Kim et al. 1988). It also hosts extended Hα emission (Buson et al. 1993; Plana

★E-mail: davor@strw.leidenuniv.nl

Table 1. Properties of NGC 2974. Note that the listed properties are taken from the Lyon/Meudon Extragalactic Database (LEDA). The distance modulus is from Tonry et al. (2001).

Parameter	Value
Morphological type	E4
M_B (mag)	−20.46
Effective B–V (mag)	1.00
PA (°)	42
Distance modulus (mag)	31.66
Distance scale (pc arcsec^{-1})	104.13

et al. 1998), and belongs to the 'rapid rotators' (Bender 1988). The total absolute magnitude of $M_B = -20.32$ puts NGC 2974 near the transition between giant ellipticals and the lower-luminosity objects that often show photometric and kinematic evidence for a significant disc component (e.g. Rix & White 1992). By combining WFPC2 imaging with TIGER integral-field spectroscopy of the central few arcsec, Emsellem, Goudfrooij & Ferruit (2003, hereafter EGF03) discovered a spiral structure in the Hα emission in the inner few arcsec, and concluded that the galaxy contains an inner stellar bar. The general properties of NGC 2974 are listed in Table 1.

The availability of both stellar and gaseous kinematics makes NGC 2974 a very interesting case for detailed dynamical modelling. Cinzano & van der Marel (1994) made dynamical Jeans models of the gaseous and stellar components, additionally introducing a stellar disc in order to fit their long-slit data along three position angles (PAs). They found that the stellar and gaseous discs were kinematically aligned and the inclination of both discs was consistent with 60°. This prompted them to suggest a common evolution, where the gas could be ionized by the stars in the stellar disc. Using more sophisticated two-integral axisymmetric models, which assume the DF depends only on the two classical integrals of motion, the energy E and the angular momentum with respect to the symmetry axis L_z, EGF03 were able to reproduce all features of the Cinzano & van der Marel (1994) data as well as their integral-field TIGER data (covering the inner 4 arcsec). The models of EGF03 did not require a thin stellar disc to fit the data.

In this paper, we construct axisymmetric models for NGC 2974 based on the Schwarzschild orbit-superposition method. This method allows the DF to depend on all three isolating integrals of motion. All previous studies with three-integral models concentrated on the determination of the mass-to-light ratio, Υ, and the mass of the central black hole, $M_{\rm BH}$. Based on the observed stellar velocity dispersion, the $M_{\rm BH}$–σ relation (e.g. Tremaine et al. 2002) predicts a central black hole mass of 2.5×10^8 M$_\odot$, which at the distance of NGC 2974 (21.48 Mpc; Tonry et al. 2001) has a radius of influence of 0.2 arcsec. Our observations of NGC 2974, with the integral-field spectrograph SAURON (Spectrographic Areal Unit for Research on Optical Nebulae; Bacon et al. 2001) do not have the necessary resolution to probe the sphere of influence of the central black hole. The dynamical models presented here are therefore aimed at the determination of Υ, the inclination, i, and the internal orbital structure. The stellar and gaseous kinematics also provide independent estimates of Υ and i, which can be used to cross-validate the results from the two approaches.

The results of the dynamical modelling are influenced by the assumptions of the models, but also by the specifics of the observations. The spatial coverage of the kinematics is one example. The 2D coverage is an improvement over a few slits often used in other studies. Similarly, increasing the radial extent of the data could change the results. Another issue, associated with the modelling techniques, is the ability of the three-integral models to recover the true DF of the galaxy. This is very important for the investigation of the internal dynamics, because the recovered orbital distribution must represent the observed galaxy if we want to learn about the galaxy's evolutionary history. In this paper we present tests designed to probe these issues and, in general, to determine the robustness of our three-integral method.

This paper is organized as follows. In Section 2 we summarize the SAURON spectroscopy and the photometric ground- and space-based data. In Section 3 we present an analysis of the velocity maps, used to quantify the presence and influence of possible non-axisymmetric motions, as well as a brief discussion on bars in NGC 2974. The three-integral dynamical models for the stellar motions are discussed in Section 4. Section 5 is devoted to tests of the three-integral method involving the determination of the model parameters (Υ, i), influence of the radial extent of the data and the recovery of the DF. In Section 6 we present the modelling of the emission-line gas kinematics and a comparison with the results of the stellar dynamical modelling. We conclude in Section 7.

2 OBSERVATIONS AND DATA REDUCTION

The observations of NGC 2974 used in this work consist of ground- and space-based imaging, and ground-based integral-field spectroscopy. The imaging data were presented in EGF03 and the absorption-line kinematics of the SAURON observations in Emsellem et al. (2004, hereafter E04) as part of the SAURON survey (de Zeeuw et al. 2002). In this paper we also use the SAURON emission-line kinematics of NGC 2974.

2.1 SAURON spectroscopy

NGC 2974 was observed with the integral-field spectrograph SAURON mounted on the 4.2-m William Herschel Telescope (WHT) in 2001 March. The observations consisted of eight exposures divided equally between two pointings, each covering the centre and one side of the galaxy. The individual exposures of both pointings were dithered to obtain a better estimate of detector sensitivity variations and to avoid systematic errors. The instrumental characteristics of SAURON and a summary of the observations are presented in Table 2.

The SAURON data were reduced following the steps described in Bacon et al. (2001) using the dedicated software XSAURON developed at Centre de Recherche Astronomique de Lyon (CRAL) Observatoire. The performed reduction steps included bias and dark

Table 2. The SAURON instrumental characteristics and exposure details of the observations of NGC 2974 obtained in 2001 March at the WHT. The sky apertures are pointed 1.9 arcmin away from the main field.

Field of view	33 × 41 arcsec^2
Aperture size	0.94 arcsec
Final spatial sampling	0.8 arcsec
Spectral range	4810–5300 Å
Spectral sampling	1.1 Å pixel^{-1}
Spectral resolution	4.2 Å (FWHM)
Number of field lenses	1431
Number of sky lenses	146
Number of exposures	8
Exposure time per pointing	1800 s
Instrumental dispersion (σ)	108 km s^{-1}
Median seeing (FWHM)	1.4 arcsec

subtraction, extraction of the spectra using a fitted mask model, wavelength calibration, low-frequency flat-fielding, cosmic-ray removal, homogenization of the spectral resolution over the field, sky subtraction and flux calibration. All eight exposures were merged into one data cube with a common wavelength range by combining the science and noise spectra using optimal weights and (re)normalization. In this process we resampled the data cube to a common spatial scale (0.8×0.8 arcsec^2) with a resulting field of view of about 45×45 arcsec^2. The data cube was spatially binned to increase the signal-to-noise (S/N) ratio over the field, using the Voronoi 2D binning algorithm of Cappellari & Copin (2003). The targeted minimum S/N was 60 per aperture, but most of the spectra have S/N ratio high (e.g. $[S/N]_{max} \approx 420$) and about half of the spatial elements remain unbinned. The final data cube of NGC 2974 and the detailed reduction procedure were presented in E04.

2.2 Absorption-line kinematics

The SAURON spectral range includes several important emission lines: Hβ, [O III]$\lambda\lambda$4959,5007 and [N I]$\lambda\lambda$5198,5200 doublets. These lines have to be masked or removed from the spectra used for the extraction of the stellar kinematics. The method most suitable for this is the direct pixel-fitting method operating in wavelength space, which allows easy masking of the emission lines. We used the penalized pixel-fitting algorithm (pPXF) of Cappellari & Emsellem (2004), following the prescriptions of E04. The line-of-sight velocity distribution (LOSVD) was parametrized by the Gauss–Hermite expansion (Gerhard 1993; van der Marel & Franx 1993). The 2D stellar kinematic maps of NGC 2974, showing the mean velocity (V), the velocity dispersion (σ), as well as higher-order Gauss–Hermite moments (h_3 and h_4), were presented in E04, along with the kinematics of 47 other elliptical and lenticular galaxies. In this paper we expand on the previously published kinematics by including two more terms in the Gauss–Hermite expansion (h_5 and h_6) to make sure all useful information is extracted from the spectra and to tighten the constraints on the dynamical models. The extraction of additional kinematic terms was performed following the same procedure as in E04. The new extraction is consistent with the published kinematics (except that now the LOSVD is parametrized with six moments) and we do not present them here explicitly (but see Fig. 12).

We estimated the errors in the kinematic measurements by means of Monte Carlo simulations. The parameters of the LOSVD were extracted from 100 realizations of the observed spectrum. Each pixel of a Monte Carlo spectrum was constructed adding a value randomly taken from a Gaussian distribution with the mean of the observed spectrum and standard deviation given by a robust-sigma estimate of the residual of the fit to the observed spectrum. All realizations provide a distribution of values from which 1σ confidence levels were estimated. During the extraction of the kinematics for error estimates, we switched off the penalization of the pPXF method in order to obtain the true (unbiased) scatter of the values (see Cappellari & Emsellem 2004, for a discussion).

2.3 Distribution and kinematics of ionized gas

NGC 2974 has previously been searched for the existence of emission-line gas. Kim et al. (1988) reports the detection of H I in a disc structure aligned with the optical isophotes. The total mass of H I is estimated to be 8×10^8 M$_\odot$, rotating in a disc with an inclination of $i \approx 55^\circ$. Buson et al. (1993) detected Hα emission distributed in a flat structure along the major axis. Assuming a disc geometry, the inferred inclination is $\approx 59^\circ$, and the total mass of H II was estimated to be $\approx 3 \times 10^4$ M$_\odot$. Similar results are found by Plana et al. (1998). Deep optical ground-based imaging studies suggested the existence of 'arm-like' spiral structures, visible in the filamentary distribution of ionized gas outside $\sim$5 arcsec (Bregman, Hogg & Roberts 1992; Buson et al. 1993). The recent high-resolution *Hubble Space Telescope* (*HST*) imaging in Hα+[N II] revealed the presence of a gaseous two-arm spiral in the inner $\sim$200 pc, with a total mass of 6.8×10^4 M$_\odot$ (EGF03).

The strongest emission line in the SAURON spectra of NGC 2974 is the [O III] doublet. There is also considerable emission in Hβ and some emission from the [N I] lines. Measurement of the emission-line kinematics followed the extraction of the absorption-line kinematics. For each spectrum in the data cube, we performed three steps, as follows.

(i) The pPXF method provided the model absorption spectrum that yielded the best fit to the spectral range with the emission lines ([O III], Hβ and [N I]) excluded.

(ii) We then subtracted the model absorption spectrum from the original observed spectrum. This resulted in a 'pure emission-line' spectrum, which was used to extract the gas kinematics.

(iii) Each emission line was approximated with a Gaussian. The fit was performed simultaneously to the three lines of [O III] and Hβ, not using the mostly negligible [N I] doublet.

This procedure assumes that the velocity and velocity dispersion of the different emission lines are equal. Performing the simultaneous fit to the lines, while allowing them to be kinematically independent, yields similar results (Sarzi et al., in preparation). Following Osterbrock (1989) we assumed a 1 : 2.96 ratio for the components of the [O III] doublet, while leaving the intensity of the [O III] and Hβ lines independent. The flux maps of the [O III] and Hβ lines as well as the maps of the [O III] emission-line mean velocity and velocity dispersion are presented in Fig. 1. The instrumental broadening of 108 km s^{-1} was subtracted in quadrature from the emission-line velocity dispersion map presented here and also used in Section 6.

Both the Hβ and [O III] emission lines are present over the whole extent of the maps in Fig. 1, but their intensity drops off approximately exponentially with distance from the centre. The [O III] emission is stronger over the entire SAURON field with the [O III] to Hβ line ratio being $\approx$1.7. The shapes of the distributions are very similar, although Hβ follows the stellar light isophotes more precisely. The [O III] distribution shows departures from the stellar isophotes in two roughly symmetric regions, positioned east and west of the centre in Fig. 1. The nature of these dips in the [O III] flux is discussed in Section 3.3.

2.4 Ground- and space-based imaging

In this study we used the existing ground- and space-based images of NGC 2974. The already reduced wide-field ground-based *I*-band image of NGC 2974 was taken from Goudfrooij et al. (1994), obtained at the 1.0-m Jacobus Kapteyn Telescope (JKT). We also retrieved the Wide Field and Planetary Camera 2 (WFPC2) association images of NGC 2974 from the *HST* archive (Program ID 6822, P. I. Goudfrooij). The details of all imaging observations are presented in Table 3.

A major complication in the derivation of the surface brightness model needed for the dynamical modelling is the existence of dust, clearly visible on the high-resolution images. We considered two possible approaches: masking the patchy dust areas and excluding these from the calculation of the model, or constructing

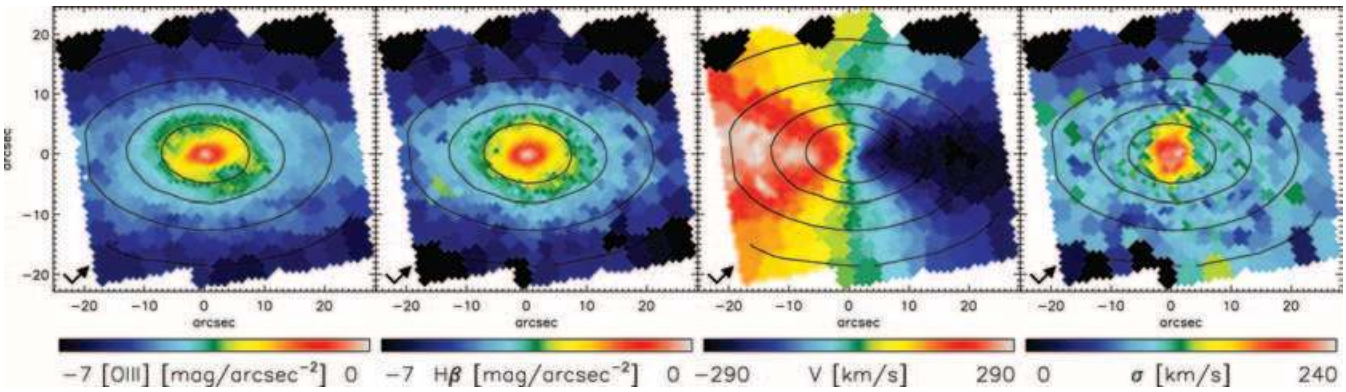

Figure 1. Distribution of Hβ and [O III] emission lines and gas kinematics observed by SAURON. Gas intensities are in mag arcsec^{-2} with arbitrary zero-points. Gas mean velocity (V) and velocity dispersion (σ) are in km s^{-1}. Overplotted contours are levels of the reconstructed total intensity from the full SAURON spectra. The arrow in the left corner of each plot marks the north-east orientation of the maps.

Table 3. Summary of the ground- and space-based observations of NGC 2974. The exposure times of the *HST*/WFPC2 observations are averages of all frames used to produce the WFPC2 association images.

	JKT	*HST*/WFPC2
Filter band	*I*	F547M and F814W
Exposure time (s)	60	700 and 250
Field of view (arcsec)	380 × 350	32 × 32
Pixel scale (arcsec)	0.3106	0.0455
Date of observations	1993/04/16	1997/04/16

a dust-corrected image. We decided to adopt the latter approach to determine the stellar surface brightness. We derived the correction of dust absorption using the F547M and F814W WFPC2 images, following the steps listed in C02. The process consists of construction of a colour excess map $E(V–I)$, from a calibrated $V–I$ colour image. The colour excess map is used to correct the pixels above a given $E(V–I)$ threshold using the standard Galactic extinction curve. We have assumed that the dust is a screen in front of the galaxy and that dust-affected pixels have the same intrinsic colour as the surrounding unaffected pixels. Fig. 2 shows the calibrated $V–I$ colour of pixels in the inner part of the PC images. The best fit to the colours was obtained by minimizing the absolute deviation of the pixel values. This fit, represented by a line in Fig. 2, was used to calculate the colour excess by subtracting the measured colour from the fit. The resulting E ($V–I$) image is shown in the second panel of Fig. 3. The other panels in the same figure present the inner parts of the F814W PC image before and after the correction of dust absorption. The colour excess image highlights the dust structure visible also in fig. 3 of EGF03, and suggests a non-uniform distribution of dust in the central region of NGC 2974.

3 QUANTITATIVE ANALYSIS OF VELOCITY MAPS

2D kinematic maps offer a large amount of information and are often superior to a few long-slit velocity profiles. The 2D nature of these data motivates us to quantify the topology and structure of these kinematic maps, just as is commonly done for simple imaging. We have developed a new technique to deal with kinematic maps based on the Fourier expansion; because of its similarity to the photometry, we have called it kinemetry (Copin et al. 2001). This method is a

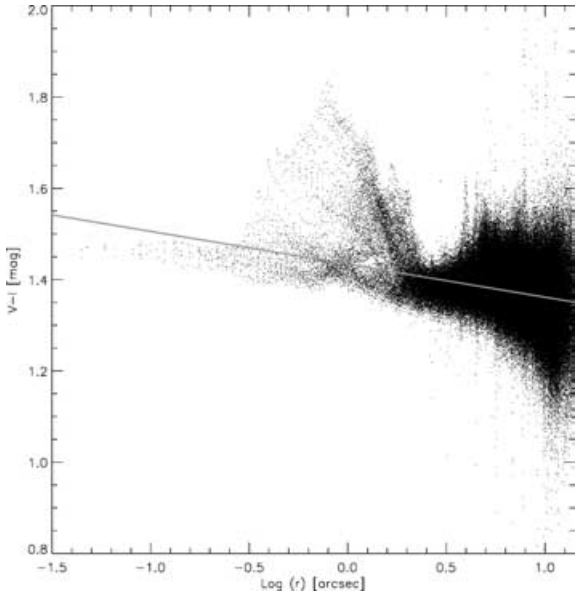

Figure 2. $V–I$ colour versus the elliptical radius of every pixel in the inner 15 arcsec of the WFPC2/PC1 images of NGC 2974. The straight line presents the best fit to the points obtained by minimizing the absolute deviation. Notice the excess of red pixels between 0.3 and 2.5 arcsec caused by dust.

generalization of the approach developed for 2D radio data (Franx, van Gorkom & de Zeeuw 1994; Schoenmakers, Franx & de Zeeuw 1997; Wong, Blitz & Bosma 2004). The aim of the method is to extract general properties from the kinematic maps of spheroidal systems (early-type galaxies) without assuming a specific intrinsic geometry (e.g. thin disc) for the distribution of stars. This changes the interpretation and the approach to the terms of the harmonic expansion from the case of cold neutral hydrogen or CO discussed in the above-mentioned papers. In this section we briefly present the method and apply it to the stellar and gaseous velocity maps (Krajnović et al., in preparation).

3.1 Harmonic expansion

The kinemetry method consists of the straightforward Fourier expansion of the line-of-sight kinematic property $K(r, \theta)$ in polar

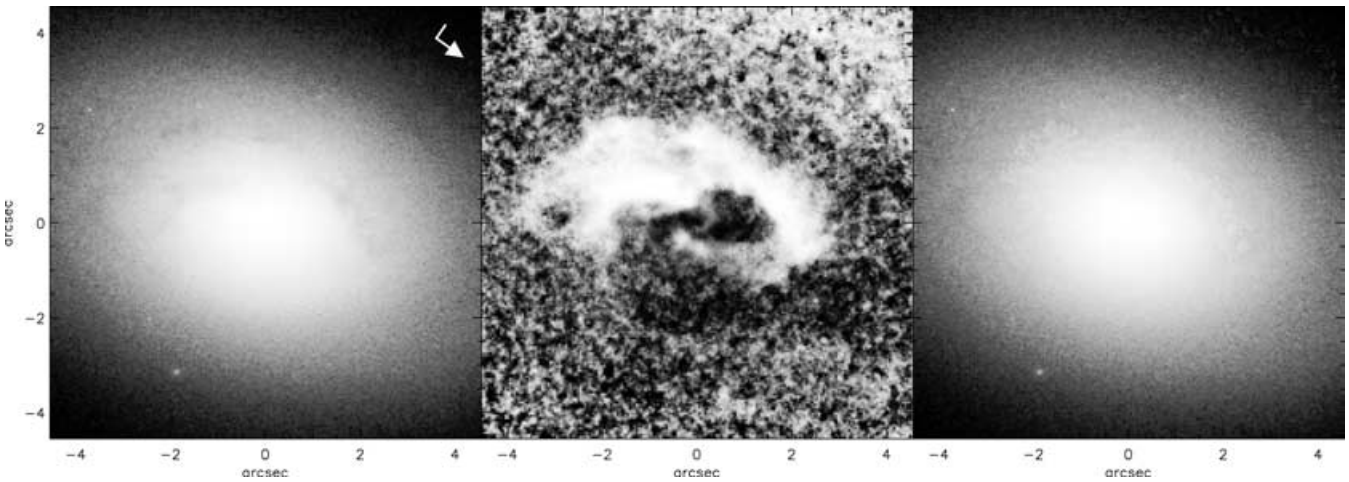

Figure 3. Dust correction on the F814W WFPC2 image of NGC 2974. From left to right: observed F814W image; colour excess $E(V–I)$ obtained as described in the text; dust corrected F814W image. The arrow points to the north and associated dash to the east. All images were constructed using histogram equalization. Lighter shades represent brighter regions. The $E(V–I)$ map is stretched between −0.1 (dark) and 0.2 (bright) magnitudes.

coordinates:

$$K(r,\theta) = a_0(r) + \sum_{n=1}^{N} c_n(r)\cos\{n[\theta - \phi_n(r)]\}. \quad (1)$$

The expansion is performed on a set of concentric circular rings (although other choices are possible), and its main advantage is linearity at constant r. The expansion is possible for all moments of the LOSVD, but in this paper we restrict ourselves to the mean velocity maps.

The kinematic moments (moments of LOSVD) of triaxial galaxies in a stationary configuration have different parity (e.g. mean velocity is odd), while the second moment $\langle v^2 \rangle$ is even. The parity of a moment generates certain symmetries of the kinematics maps. More generally, the maps of odd moments are point-antisymmetric, or

$$V(r,\theta+\pi) = -V(r,\theta). \quad (2)$$

If axisymmetry is assumed, in addition to the previous relation, maps are mirror-antisymmetric, or

$$V(r,\pi-\theta) = -V(r,\theta). \quad (3)$$

These symmetry conditions translate into the requirement on the harmonic expansion (equation 1) that for point-antisymmetric maps the even coefficients in the expansion are equal to zero, while in the case of mirror-antisymmetry, additionally, the odd phase angles have a constant value, equal to the photometric PA of the galaxy in the case of a true axisymmetric galaxy. This means that to reconstruct the mean velocity map of a stationary triaxial galaxy, it is sufficient to use only odd terms in the expansion.

These properties of the velocity maps enable certain natural filtering – point-(anti)symmetric (equation 2) and mirror-(anti)symmetric (equation 3) – using the harmonic expansion with coefficients set to zero or phase angles fixed at certain values. For (visual) comparisons of the data with the results of axisymmetric modelling, it is useful to apply the axisymmetric filtering to the data, as we see below (Section 6).

3.2 Kinemetric analysis of velocity maps

We wish to know the intrinsic shape of NGC 2974 and, in particular, whether it is consistent with axisymmetry, which would permit the construction of three-integral axisymmetric dynamical models of the galaxy. In order to obtain the necessary information, we applied the kinemetric expansion to the observed stellar velocity map. If NGC 2974 is an axisymmetric galaxy, the kinemetric terms should have odd parity (even terms should be zero) and the kinematic PA should be constant and equal to the PA.

The amplitude and phases of the first five terms in the expansion are presented in Fig. 4. Fig. 4(a) presents the dominant term in the expansion, c_1, which gives the general shape and amplitude of the

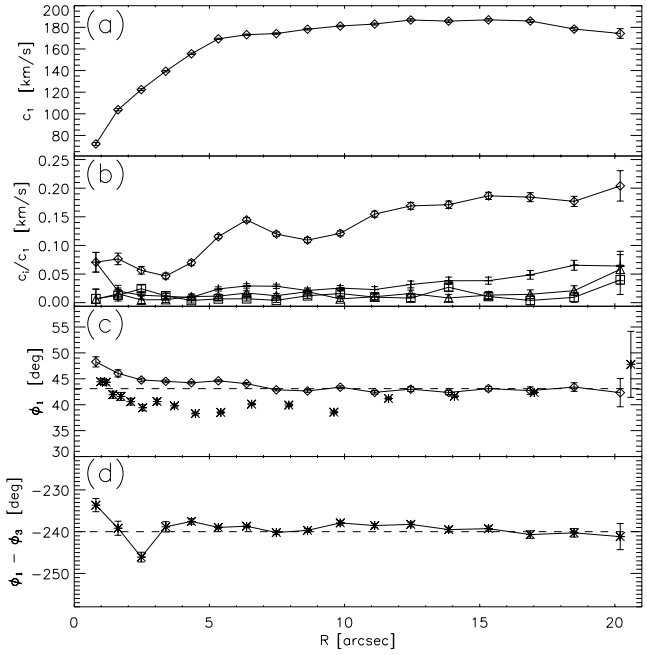

Figure 4. Kinemetric expansion of the stellar velocity map as a function of radius. (a) First amplitude coefficient in the harmonic expansion c_1. (b) Ratios of amplitude coefficients presented by triangles for c_2/c_1, diamonds for c_3/c_1, squares for c_4/c_1 and plus signs for c_5/c_1. (c) Important PAs: phase angle ϕ_1 representing the kinematic PA (diamonds), photometric PA as measured on WFPC2/PC1 F814W image (asterisks) and adopted value for photometric PA measured from the integrated SAURON flux image (dashed straight line). (d) Difference between the first and third phases from the kinemetric expansion.

stellar velocity map. The correction to this term is given by the next significant term, c_3, which is already much smaller than c_1 and is presented in Fig. 4(b) as a fraction of c_1. Even terms in the expansion, c_2 and c_4, are also plotted in the same panel, and are much smaller ($\sim$1 per cent of c_1).[1] For comparison, the fifth term in the expansion, c_5, is also plotted and is larger than both c_2 and c_4. The SAURON pixel size is $\sim$1 arcsec and measurement of higher-order terms at radii smaller than 2 arcsec cannot be trusted. Clearly, the velocity map in NGC 2974 can be represented by the first two odd terms in the expansion. Neglecting all higher terms results at most in an error of a few per cent.

Figs 4(c) and (d) present the phases of the dominant terms. The ϕ_1 phase is defined as the kinematic angle of the velocity map, here measured east of north. This angle is compared with measurements of two important angles: (i) the PA measured on the WFPC2/PC F814W dust-corrected image using the IRAF ellipse fitting task ELLIPSE; (ii) the PA measured on the reconstructed SAURON flux image obtained by integrating the spectra in each bin. The agreement between the different angles measured on the SAURON observations is excellent, with slight departures in the inner 3 arcsec. The PA measured on the high-resolution WFPC2 image suggests a small photometric twist in the inner 10 arcsec of $\approx 3^\circ$, which can be also seen in Fig. 10.

The phase angle ϕ_3 is the phase of the third term in the kinemetric extraction. It is easy to show, if the galaxy is axisymmetric [requiring in equation 1, $K(r, \theta) = 0$ for $\theta = \phi_1 + \pi/2$], and the higher terms can be neglected, that the phases ϕ_1 and ϕ_3 satisfy the relation

$$\phi_1 - \phi_3 = \frac{n\pi}{3} \tag{4}$$

where $n \in \mathbb{Z}$. The last panel in Fig. 4 shows this phase difference. The condition given by equation(4) is satisfied along the entire investigated range with a small deviation in the inner 3 arcsec. Summarizing all the above evidence, we conclude that the observed stellar kinematics in NGC 2974 is consistent with axisymmetry.

We repeated the kinemetric analysis[2] on the emission-line gas velocity maps, and we present the results in Fig. 5. While the amplitude coefficients, c_i, are similar to the stellar coefficients (small values of all terms higher than c_3), the behaviour of the phase angles is quite different.

Fig. 5(d) is perhaps the best diagnostic tool. The dashed line presents the required value for the difference between the phase angles, $\phi_1 - \phi_3$, assuming axisymmetry. Deviations are present in the inner 4 arcsec and, although much smaller, between 9 and 11 arcsec. These deviations indicate departures from axisymmetry, which are strongest in the central few arcsec.

3.3 Signature of bars in NGC 2974

In the previous section, we quantified the signatures of non-axisymmetry on the gas velocity maps, especially strong in the inner 4 arcsec. Inside this radius, EGF03 discovered a two-armed spiral and explained it by a weak bar with the corotation resonance (CR) at 4.9 arcsec and outer Lindblad resonance (OLR) at 8.5 arcsec. These scales are consistent with the observed departures from axisymmetry in the SAURON kinematic maps. An additional confirmation

[1] The zeroth term, a_0, gives the systemic velocity of the galaxy and is not important for this analysis.

[2] A similar analysis approach for a gas disc would be using the Schoenmakers et al. (1997) harmonic analysis on a tilted-ring model of the gas disc, interpreting the results within epicycle theory (see also Wong et al. 2004).

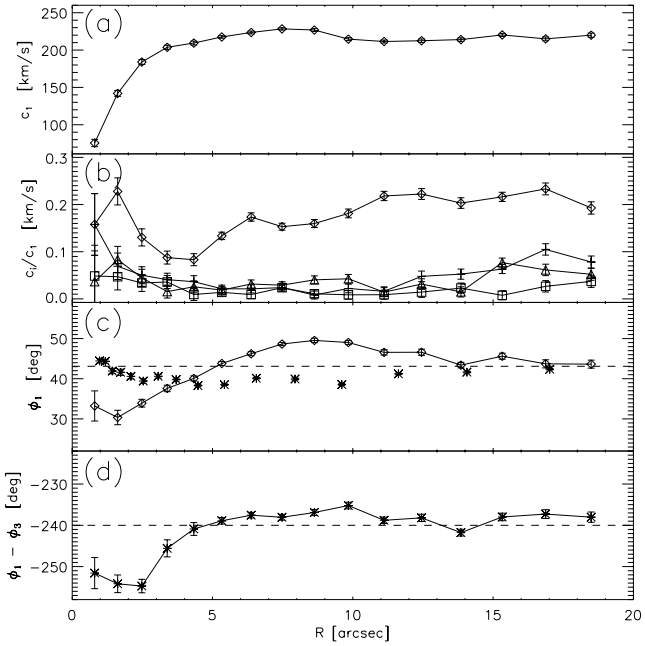

Figure 5. Same as Fig. 4, but for the gas velocity map.

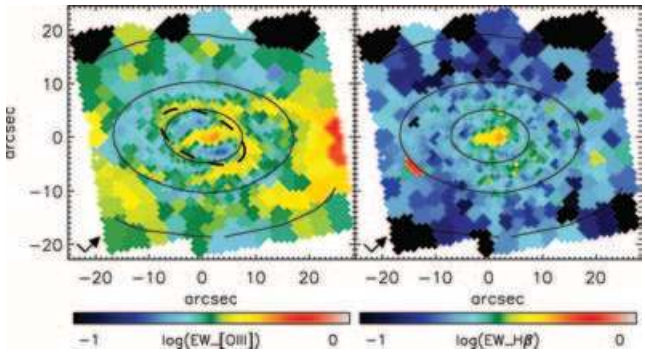

Figure 6. Equivalent widths of [O III] and Hβ emission lines. These plots, constructed by dividing the emission-line flux by the symmetrized stellar continuum, show the relative distribution of emission lines to the stellar continuum. The dashed ellipse represents the possible OLR ring of the inner bar (see text for details). Overplotted contours are levels of the reconstructed total intensity from the full SAURON spectra. The arrow in the left corner of each plot marks the north-east orientation of the maps.

comes from the equivalent width maps of emission lines (Fig. 6). These maps show the distribution of the emission lines relative to the stellar continuum. Especially noticeable is the ring structure in the [O III] equivalent width distribution. For comparison, we overplotted an ellipse with semimajor axis length of 8.5 arcsec (the radius of the OLR of the EGF03 bar). The orientation ($\sim 25^\circ$ away from the major axis of the galaxy) and the size of the ring ($\sim$8.5 arcsec) are in good agreement with the expected characteristics of the bar discovered by EGF03.

The equivalent width maps show that the [O III] emission line is also influenced outside the OLR. There is an increase in the value of the equivalent width at larger radii as well as a filamentary (spiral) structure connecting the ring and this large-scale region. Also, as seen before in Fig. 1, the distribution of the [O III] emission-line intensity exhibits an elongated structure in the central 5 arcsec. Similarly, around 8–10 arcsec [O III] is also elongated, but this time

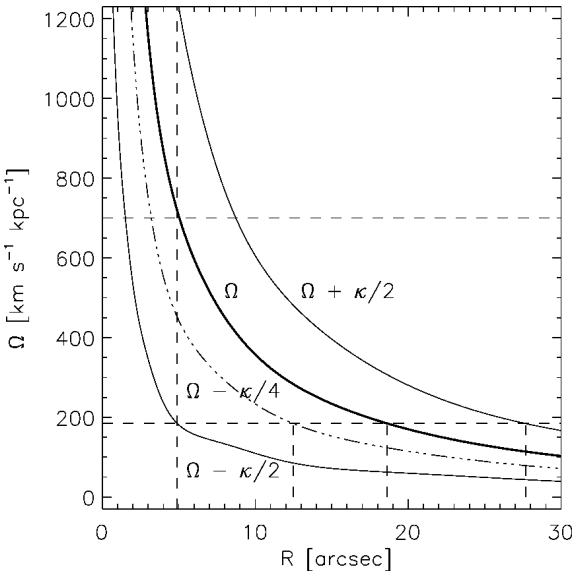

Figure 7. Diagram of resonances in NGC 2974, derived from the potential of the best-fitting stellar dynamical model. The upper horizontal line is the pattern speed of the nuclear (secondary) bar from the EGF03 study (Ω_p^s = 700 km s^{-1} kpc^{-1}). The lower horizontal line shows the position of the inferred pattern speed of the large-scale primary bar (Ω_p^p = 185 km s^{-1} kpc^{-1}). The vertical lines show the assumed radial positions of important resonances of the primary bar. From left to right: ILR (CR of the secondary bar), UHR, CR and OLR.

approximately perpendicular to the first elongated structure. Following this, the [O III] map has a plateau between 12 and 15 arcsec. The end of the plateau is followed by a dip in the distribution with a possible turn-up at radii larger than 20 arcsec.

Although the central structure and kinematics of the [O III] distribution are influenced by the inner bar, the large-scale structure (beyond ≈10 arcsec) is not likely to be influenced by this weak inner bar. On a more speculative basis, we can infer the existence of a large-scale bar. Studies of double bars (Erwin & Sparke 2002, 2003; Laine et al. 2002) suggest a size ratio of about 5–10 between the primary and secondary bars; this would set the size of a hypothetical large-scale (primary) bar in NGC 2974 to between about 12.5 and 25 arcsec.

A more precise, although still approximate, estimate of the properties of the primary bar can be obtained from the resonance curves of NGC 2974. Using the potential of the best-fitting stellar dynamical model (see Section 4) we constructed the resonance diagram presented in Fig. 7. We calculated profiles of Ω, $\Omega - \kappa/2$, $\Omega + \kappa/2$ and $\Omega - \kappa/4$, where Ω is the angular velocity, V/r, and κ is epicyclic frequency, defined as $\kappa^2 = r\,(\mathrm{d}\Omega^2/\mathrm{d}r) + 4\Omega^2$. Assuming that the resonances of the primary and secondary bars are coupled to minimize the chaos produced around the resonances (Pfenniger & Norman 1990; Friedli & Martinet 1993), where the inner Lindblad resonance (ILR) of the primary bar is the CR of the secondary bar, we can estimate the main resonances of the primary bar (indicated by the vertical lines in Fig. 7). The pattern speed of the primary component is then ≈185 km s^{-1} kpc^{-1}, the ILR is at 4.9 arcsec, the ultraharmonic resonance (UHR) at ≈12.5 arcsec, the CR at ≈18.6 arcsec and the OLR at ≈27.7 arcsec. The size of the primary bar can be taken to be 80 per cent of its CR, so about 13–14 arcsec (∼1.4 kpc).

The presented analysis is strictly valid only for an axisymmetric potential with a weak bar perturbation; hence, the above-mentioned

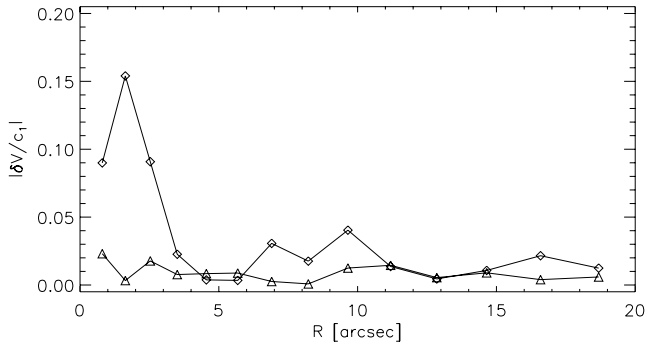

Figure 8. Contribution of the non-axisymmetric motion to the stellar and gaseous velocity maps, as a fraction of the dominant term in the kinemetric expansion, c_1. Diamonds represent the emission-line gas velocity contribution, while triangles denote the stellar velocity contribution.

size estimates are only approximate, but indicative. We see several features in the [O III] distribution and velocity maps that support the assumption of a large-scale primary bar: the dip in the gas velocity map around 12 arcsec, the plateau between 12 and 15 arcsec in the [O III] distribution, as well as the dip in the [O III] distribution around 18 arcsec. The last feature corresponds to the position of the CR, which is a chaotic region devoid of gas, consistent with the observed lower flux in that region.

3.4 Case for axisymmetry in NGC 2974

The alignment of the gaseous and stellar components, previously detected and also confirmed in this study, suggests that NGC 2974 is an axisymmetric galaxy. However, the gaseous component shows signatures of non-axisymmetric perturbations. The contribution of the non-axisymmetric motion, $\Delta V/c_1$, to the total velocity field can be quantified from the phase difference $\phi_3 - \phi_1$. If the condition in equation (4) is not satisfied, then

$$\frac{\Delta V}{c_1} = \frac{c_3}{c_1} \sin 3(\phi_1 - \phi_3), \tag{5}$$

which is presented in Fig. 8 for both stellar and gaseous velocity maps. At ∼3 arcsec, $\Delta V/c_1$ for the emission-line gas is ≈0.1 and at ∼10 arcsec it is ≈0.04, confirming that the non-axisymmetric contribution is significant in the centre of the emission-line velocity map. Its influence on the stellar velocity is not significant over the SAURON field. Emission-line gas is a more responsive medium and, unlike the stars, because of the viscosity of the gas particles, shows evidence of weak non-axisymmetric perturbations. It is possible that other early-type galaxies with disc-like components harbour such weak and hidden bar systems.

Summarizing, the stellar velocity map is point-antisymmetric and mirror-antisymmetric, supporting an axisymmetric shape for NGC 2974. On the other hand, the gaseous velocity map shows strong deviations from mirror-antisymmetry in the centre, and the distribution and equivalent width of [O III] emission lines support the weak inner bar found by EGF03 and suggest the existence of a weak large-scale bar. However, because the bar perturbations on the axisymmetric potential are presumed to be weak and do not appear to influence the stellar kinematics, we ignore them in the remainder of the paper, and we describe NGC 2974 with an axisymmetric potential.

4 STELLAR DYNAMICAL MODELLING

In order to investigate the orbital structure of NGC 2974, we construct fully general axisymmetric models of the galaxy's stellar

component. The three-integral models presented here are based on the Schwarzschild orbit-superposition method (Schwarzschild 1979, 1982), further developed by Rix et al. (1997), van der Marel et al. (1998) and Cretton et al. (1999), and adapted for more general surface-brightness distributions by C02 and V02, similarly as in Cretton & van den Bosch (1999). The three-integral modelling technique is widely used for constructing dynamical models of axisymmetric galaxies, and has been thoroughly described in the literature by the aforementioned authors as well as by other groups (e.g. Gebhardt et al. 2003; Valluri, Merritt & Emsellem 2004). It is most commonly used to determine the masses of the central black holes in nearby galaxies and to investigate the internal orbital structure of the galaxies. The SAURON observations of NGC 2974 do not have the necessary resolution to probe the sphere of influence of the central black hole, and we therefore restrict ourselves to the determination of the mass-to-light ratio Υ and the inclination i of the galaxy, as well as the internal orbital structure.

4.1 MultiGaussian expansion mass model

The starting point of the stellar dynamical modelling is the determination of the gravitational potential of the galaxy. The potential can be obtained by solving the Poisson equation for a given density distribution, which can be derived by deprojecting the observations of the 2D stellar surface density. In this work we used the multi-Gaussian expansion (MGE) method (Emsellem, Monnet & Bacon 1994), following the approach of C02 and V02.

In order to obtain the MGE model, we simultaneously fitted the ground-based I-band image and the dust-corrected PC part of the WFPC2/F814W image using the method and software developed by Cappellari (2002). The dust correction (Section 2.4) successfully removed the dust contamination from the high-resolution image of the nucleus, but the large-scale image was badly polluted by several stars, with a particularly bright star almost on the galaxy's major axis. We masked all stars inside the model area to exclude them from the fit. The ground-based image, used to constrain the fit outside 25 arcsec, was scaled to the WFPC2/PC1 image. We computed the point spread function (PSF) of the F814W PC1 image at the position of the nucleus of NGC 2974, using the TINYTIM software (Krist & Hook 2001), and parametrized it by fitting a circular MGE model with constant PA as in C02. Table 4 presents the relative weights G_j (normalized such that their sum is equal to unity) and the corresponding dispersions σ of the four Gaussians. Table 5 gives the parameters of the MGE model analytically deconvolved from the PSF. Following the prescription of Cappellari (2002), we increased the minimum axial ratio of the Gaussians, q_j, until the χ^2 changed significantly, in order to make as large as possible the range of allowed inclinations by the MGE model. The upper limit to q_j was also constrained such that the MGE model was as close as possible to a density stratified on similar ellipsoids. Although the deprojection of an axisymmetric density distribution is non-unique (Rybicki 1987), our 'regularization' on the MGE model produces realistic intrinsic densities, while preventing sharp variations, unless they are required to fit the surface brightness. We have verified that the MGE model used in this study is consistent with the MGE model presented in EGF03.

Table 4. The MGE parameters of the circular PSF of the *HST*/WFPC2/F814W filter.

j	G_j	σ_k (arcsec)
1	0.352	0.024
2	0.531	0.072
3	0.082	0.365
4	0.035	0.908

Table 5. The parameters of the MGE model of the deconvolved I-band WFPC2 surface brightness of NGC 2974. Columns present (from left to right) the number of the 2D Gaussian, the central intensity of the Gaussian, the width (sigma) of the Gaussian, the axial ratio of the Gaussian and the total intensity contained in the Gaussian.

j	$I_j(L_\odot\,\mathrm{pc}^{-2})$	σ_j (arcsec)	q_j	$L_j(\times 10^9 L_\odot)$
1	190297.	0.0378596	0.580000	0.0108
2	44170.6	0.0945030	0.800000	0.0215
3	24330.8	0.185143	0.800000	0.0455
4	27496.3	0.340087	0.583279	0.1264
5	23040.6	0.591227	0.720063	0.3952
6	10299.6	1.15500	0.777448	0.7279
7	5116.29	3.41758	0.658664	2.6820
8	1902.25	8.67562	0.597636	5.8305
9	388.278	17.5245	0.677645	5.5060
10	139.447	43.9864	0.580000	10.663
11	16.9405	82.9488	0.800000	6.3538

The comparison between the MGE model and the photometry along different angular sectors is shown in Fig. 9. The profiles are reproduced to within 3 per cent, and the rms error is about 2 per cent. The increase of the relative error (right-hand panel in Fig. 9) at larger radii is caused by the light pollution of the bright star on the major axis of the galaxy, and can be better understood by looking at the comparison of the convolved model and the actual observation. Fig. 10 presents both ground- and space-based images and the MGE model. On the WFPC2/PC image there is a slight deviation from the model (of constant PA) about 10 arcsec from the nucleus. The deviating structure is point-symmetric and reminiscent of a spiral perturbation, as suggested by other studies (Bregman et al. 1992; Buson et al. 1993; EGF03). Except for this slight departure from the model, the galaxy surface brightness is well represented by the MGE model and we use it to calculate the representative gravitational potential.

4.2 Construction of three-integral models

Briefly, the Schwarzschild method can be divided into four steps. In the first step, the stellar potential is derived, assuming the shape of the potential (axisymmetry) and stellar mass-to-light ratio, Υ (free parameter), through deprojection of a parametrization of the surface density (in this case, MGE parametrization which can be deprojected analytically). The second step involves the construction of a representative orbit library by integrating the orbits in the derived potential. Each orbit is specified by three integrals of motion (E, L_z and I_3), where E is the energy, L_z is the component of the angular momentum along the z symmetry axis, and I_3 is a non-classical integral, which is not known analytically. The integral space is constructed on a grid that includes >99 per cent of the total luminous mass of the galaxy. The next step consists of projecting the orbits on to the space of observables (x', y', $v_{\rm los}$), where (x', y') are in the plane of the sky and $v_{\rm los}$ is the line-of-sight velocity given by the observations. In our implementation, this is done by taking into account the PSF convolution and aperture binning. The final step of the method is to determine the set of weights for each orbit that, when added together, best corresponds to the observed

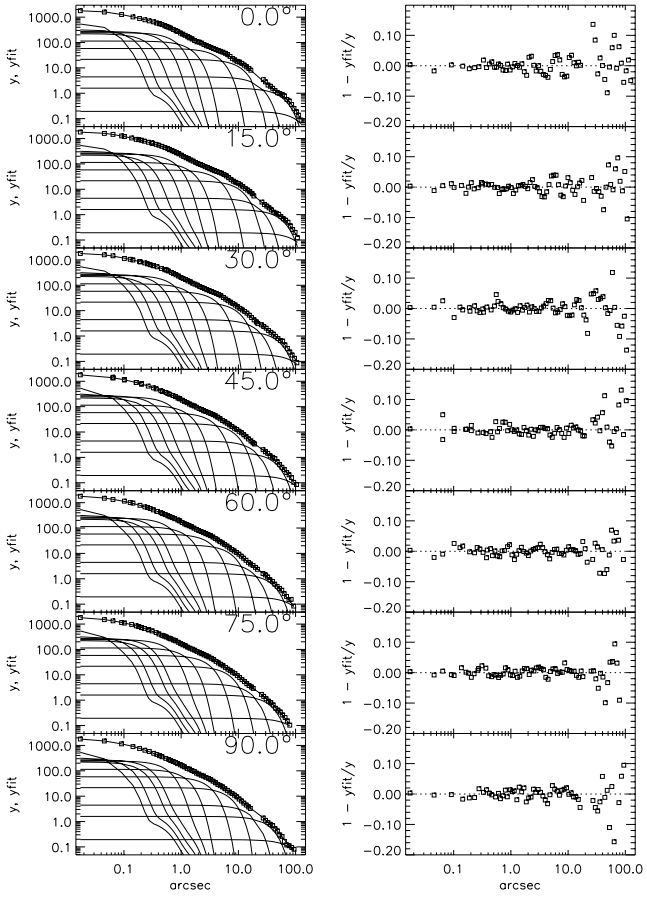

Figure 9. Left panels: comparison between the combined WFPC2/F814W and ground-based photometry of NGC 2974 (open squares) and the MGE model (solid line) in seven angular sectors as a function of radius. The individual convolved Gaussians are also shown. Right panels: radial variation of the relative error along the profiles.

kinematics in the given spatial bin as well as reproducing the stellar density. In our implementation of the method, this best-fitting set is found by solving a non-negative least-squares problem using the routine written by Lawson & Hanson (1974).

The software implementation used here is similar to that used in the studies of V02 and C02, but it has evolved substantially since. The improvements are described in detail in Cappellari et al. (in preparation). We have verified that the results from the new code are the same as those from the old code if identical settings are adopted. An application to the elliptical galaxy NGC 4473 was presented in Cappellari et al. (2004). Here we give a quick overview of the changes with respect to the description in C02.

(i) The method requires that the orbits sample a three-dimensional space of integrals of motion, the energy E, L_z and I_3. In the new scheme (see Cretton et al. 1999 for details of the previous approach), at each E, we construct a polar grid of initial starting positions on the meridional plane (linear in angle and in radius), going from $R = z = 0$ to the curve defined by the thin tube orbits (to avoid duplication), which is well approximated by the equation $R^2 + z^2 = R_c^2(E)$, where $R_c(E)$ is the radius of the circular orbit at energy E. The orbits are released with $v_R = v_z = 0$ and $L_z \neq 0$. In this way, we sample the observable space by uniformly distributing the position of the orbital cusps (see Cappellari et al. 2004) on the sky plane.

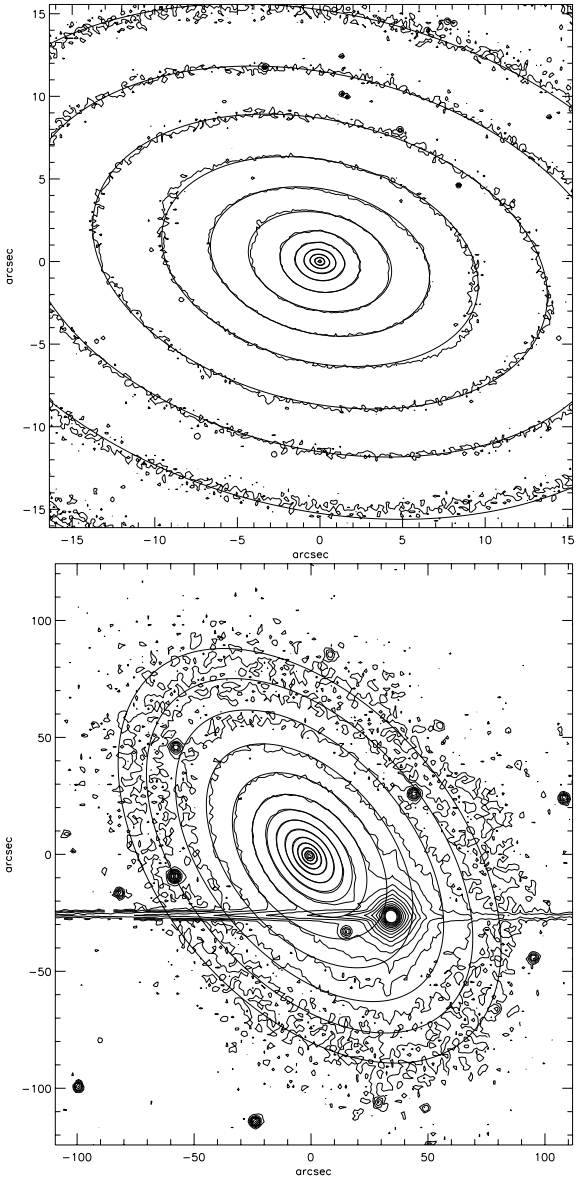

Figure 10. Contour maps of the ground-based I-band and dust-corrected WFPC2/F814W images. The brightest star on the ground-based image as well as four additional stars covered by the model were masked out and excluded from the fit. Superposed on the two plots are the contours of the MGE surface brightness model, convolved with the WFPC2 PSF.

(ii) Improved treatment of seeing effects and instrumental PSF by a Monte Carlo method. The PSF can be considered as the probability that an observed photon arriving at a detector will be displaced from its original position by a given amount (specified by the PSF characteristics). The projected orbital points (results of the orbit integration and projection on to the sky plane) are stored in the apertures in which they landed, after applying a random displacement taken from the Gaussian probability distribution defined by the PSF.

(iii) Generalization of the projection of the orbits into the space of the observables. The bins of the optimal Voronoi binning of the 2D integral-field data have non-rectangular shapes. The orbital observables now can be stored on apertures of any shape that can be represented by polygons.

4.3 Stellar dynamics: modelling results and discussion

Our stellar kinematic maps of NGC 2974 consist of 708 Voronoi bins. Each bin contributes with six kinematic observables to which we also add the intrinsic and projected mass density observables, resulting in a grand total of 5664 observables. The largest orbit library that was computationally possible for the given number of observables consists of $2 \times 41 \times 10 \times 10 = 8200$ orbits (for each of the 41 different E we construct a polar grid of starting points sampling 10 angles and 10 radii). With this choice of orbit library, the number of observables is smaller than the number of orbits, and the non-negative least-squares fit will not have a formally unique solution. Moreover, the recovery of the orbital weights for the orbits from the observations is an inverse problem, and as such is intrinsically ill-conditioned. For these reasons, a direct solution of the problem generally consists exclusively of sharp isolated peaks. It is unlikely for the DF of real galaxies to be very jagged, because (violent) relaxation processes tend to smooth the DF. Moreover, observational constraints on the smoothness of the DF, at least for the bulk of the stars in a galaxy, come from the smoothness of the observed surface brightness, down to the smallest spatial scales sampled by the *HST*.

A standard mathematical approach to solve inverse problems is by regularizing (e.g. Press et al. 1992, chapter 18). This has been generally applied by all groups involved in this modelling approach (e.g. Rix et al. 1997; Gebhardt et al. 2003; Cretton & Emsellem 2004; Valluri et al. 2004). Regularization inevitably biases the solution, by forcing most orbits to have a non-zero weight. The key here is to apply the right amount of regularization. Previous tests with the Schwarzschild code suggested a value of the regularization parameter $\Delta = 4$ (see Cretton et al. 1999; V02). After initial testing we also adopted this value. For more details on regularization, see McDermid et al. (in preparation).

The models are axisymmetric by construction. In order to avoid possible systematic effects, we additionally symmetrize the stellar kinematics, as usually done in other studies. The symmetrization uses the mirror-(anti)symmetry of the kinematic fields, such that kinematic values from four symmetric positions $[(x, y), (x, -y), (-x, y), (-x, -y)]$ were averaged. However, the Voronoi bins have irregular shapes and they are not equally distributed with respect to the symmetry axes of the galaxy (minor and major axes). In practice, we average the four symmetric points, and if for a given bin there are no bins on the symmetric positions, we interpolate the values on those positions and then average them. As the number of data points is not decreased in this way, the errors were left unchanged.

Finally, we fitted axisymmetric dynamical models to symmetrized observations of velocity, velocity dispersion and Gauss–Hermite moments (h_3–h_6) while varying the mass-to-light ratio Υ and the inclination i. Fig. 11 shows a grid of our models with overplotted $\Delta\chi^2$ contours. The best-fitting parameters are $\Upsilon = 4.5 \pm 0.1$ (in the I band) and $i = 65^\circ \pm 2.^\circ5$. The data–model comparison for these values is given in Fig. 12 (symmetrized data are shown in the first row and the best-fitting model in the third row). In the same figure we present the best-fitting models for the given inclinations. The formal statistical analysis firmly rules out (with 3σ confidence) all inclinations outside $i = 65^\circ \pm 2.^\circ5$. The differences between the models are only marginally visible in Fig. 12. However, comparing the models with the top row of symmetrized data, it is noticeable that the velocity dispersion is less well fitted with increasing inclination. On the other hand, the fit to h_3 improves with higher inclinations. Higher-order moments change similarly and the final χ^2 is the result of this combined effect. Surprisingly, the difference between the best-fitting model and the data is bigger than the difference between the other models and the best-fitting model, provoking the question whether the determination of the inclination is robust.

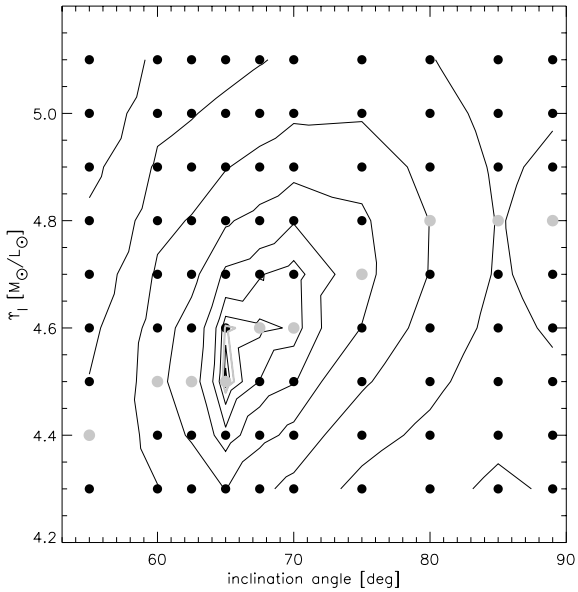

Figure 11. A grid of inclination angle i versus M/L ratio Υ. Contours present constant $\Delta\chi^2$, measuring the goodness of fit of the dynamical models. Every symbol corresponds to a three-integral axisymmetric model with given inclination angle and Υ ratio. The best-fitting models for each inclination are presented with grey symbols. The first three contours show the formal 68.3, 95.4 and 99.73 per cent (thick grey contour) confidence regions for two degrees of freedom. The best-fitting model on the grid has an inclination of 65° and $\Upsilon = 4.5$.

Recently, EGF03 used two-integral $f(E, L_z)$ dynamical models and found a best fit for an inclination of 60°; however, they also stated that models with $58^\circ \leqslant i \leqslant 65^\circ$ fit equally well. Our three-integral models have a larger freedom in fitting the observations and it is unknown whether these models can uniquely constrain the inclination. Our obtained inclination is close to the previous measurements in the literature (references in Sections 1 and 2), and also to the inclination measured from gas and dust. NGC 2974 is perhaps a special case (in terms of its intrinsic structure and geometry) for which three-integral models are able to give a stronger constraint on the inclination. We return to this issue in Section 5.2.

The integral space of the best-fitting model [i.e. the space defined by the isolating integrals of motion (E, L_z, I_3) that define the orbits and the DF $f = f(E, L_z, I_3)$] is shown in Fig. 13. Each panel presents mass assigned to orbits of constant energy, parametrized by the radius of the circular orbit. This orbit also has the maximum angular momentum, and circular orbits of negative and positive angular momentum are in the bottom-left and bottom-right corners of each plot, while the low angular momentum orbits are close to the symmetry (y) axis. An interesting feature dominates the panels with radii larger than 5.11 arcsec. A high fraction of mass is assigned to orbits with high angular momentum. This indicates that the bulk of the stars between these radii rotate with high angular momentum. A possible physical interpretation is that a large fraction of the stars orbit in a disc. Cinzano & van der Marel (1994) argued that NGC 2974 has an embedded stellar disc, and in their two-integral Jeans models they were not able to fit the stellar kinematics without introducing a disc with $\approx$7 per cent of the total galaxy light. On the other hand, the two-integral models of EGF03 did not need to invoke an additional stellar disc component to fit data consisting

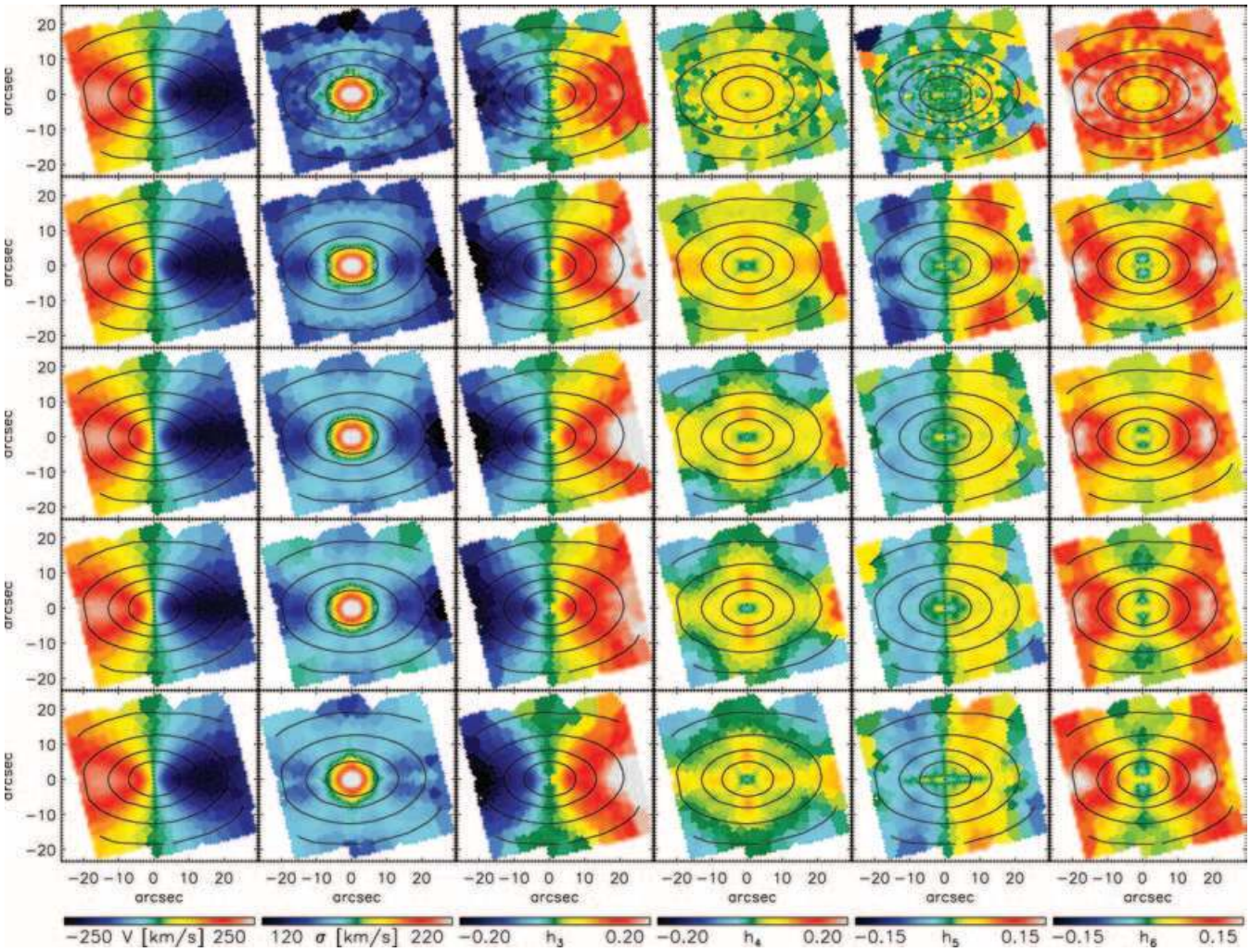

Figure 12. Comparison of the symmetrized observation of NGC 2974 (first row) and four orbital superposition models with best mass-to-light ratio Υ, for a given inclination i. From second row to bottom, $(i, \Upsilon) = (55, 4.4)$, $(65, 4.5)$, $(75, 4.7)$, $(89, 4.8)$. From left to right, each panel presents mean velocity (V), velocity dispersion (σ) and Gauss–Hermite moments (h_3, h_4, h_5 and h_6). Isophotal contours of total light are shown with solid lines.

of their TIGER data and the three long slits of Cinzano & van der Marel (1994). The integral space presented here suggests that the three-integral models need orbits with high angular momentum, but the selected orbits also have different values of I_3, and therefore do not represent a very thin stellar disc as assumed by Cinzano & van der Marel (1994), but a somewhat flattened distribution of stars as in a normal S0. The relative light contribution of the high angular momentum orbits is $\approx$10 per cent, which corresponds to a total stellar mass of 1.5×10^{10} $M_\odot$ assuming the best-fitting model inclination and Υ.

5 TESTS OF THE SCHWARZSCHILD ORBIT-SUPERPOSITION MODELS

In the previous section we used three-integral models to recover the inclination, the mass-to-light ratio and the internal structure of NGC 2974. Surprisingly, we find that the inclination is tightly constrained by χ^2 contours (Fig. 11), although the difference between the models (Fig. 12) is smaller than the difference between formally the best-fitting model and the data. In this section, we wish to test the robustness of these results as well as the general ability of the three-integral models to recover the given parameters. For this purpose we constructed an axisymmetric model mimicking NGC 2974 using two integrals of motion: the energy, E, and the z-component of the angular momentum, L_z. This two-integral galaxy model has the advantage of a known DF, $f = f(E, L_z)$, everywhere, which we want to compare with the results of the three-integral modelling. There are three issues we wish to test, as follows.

(i) Recovery of the input parameters of the two-integral model galaxy. This is a general test to show whether the three-integral method can recover the parameters used in construction of a test model. We wish to be consistent with the observations and consider only the recovery of the input mass-to-light ratio and inclination, especially in light of the results from Section 4.

(ii) Influence of the spatial coverage. The SAURON kinematic observations of NGC 2974 roughly cover one effective radius. This is also the typical size of most kinematic observations of other early-type galaxies from the SAURON sample. Here we want to test the influence of the limited extent of the kinematic coverage on the recovery of the orbital distribution. We do this by comparing the difference between models using a limited and a full spatial kinematic information provided by the two-integral galaxy model.

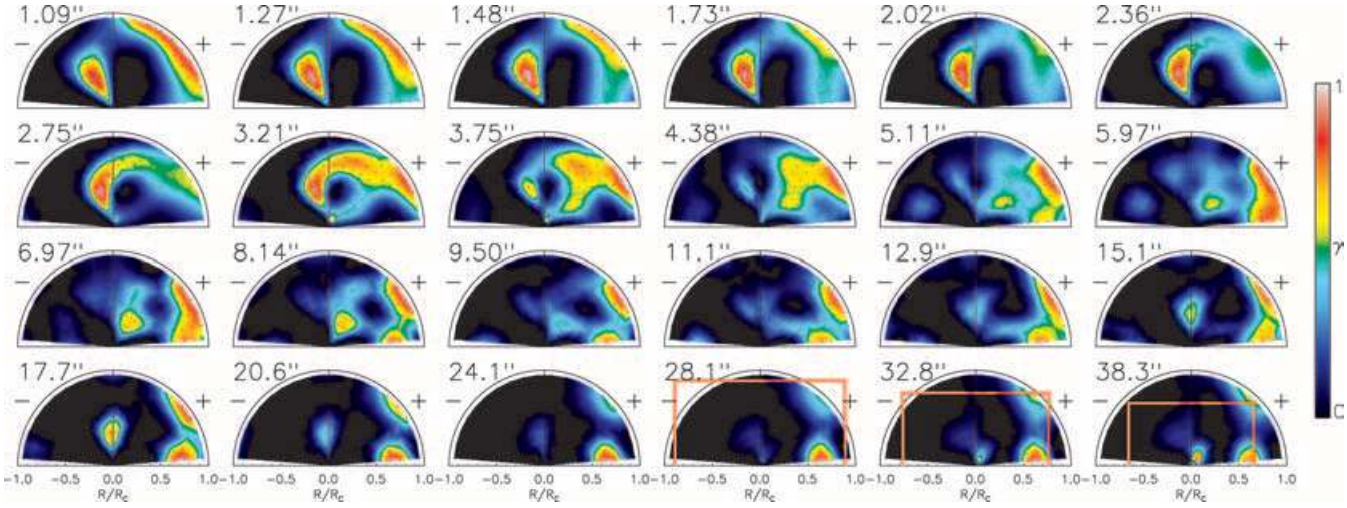

Figure 13. Integral space of the best-fitting orbit-superposition model for NGC 2974. Each panel plots the meridional plane (R, z) with the starting positions of orbits (dots) for the given energy. Orbital starting positions correspond to the position of cusps ($v_R = v_z = 0$). Overplotted is the fraction of mass assigned to orbits at constant energy, labelled by the radius of the circular orbit in arcsec (given in the upper-left corner of each panel). The radius of the circular orbit is the size of the horizontal axis (measured from the centre). Negative values are obtained by sign reversal, because orbits can be prograde and retrograde. Orbits with high angular momentum are found in the right and left corners, respectively, on the plots. We show only the radii constrained by the data. The last three panels have the size of the SAURON field overplotted for comparison (red rectangle). The area inside the rectangle is constrained by the kinematic data. The colour bar on the right represents the relative colour coding of the orbital mass weights (γ), where 1 represents the largest mass weight assigned to an orbit at the given energy.

(iii) The recovery of the input DF. We wish to test the ability of our three-integral models to correctly recover the true input (two-integral) DF. Similar tests were also presented by Thomas et al. (2004) for their implementation of the Schwarzschild method. Cretton et al. (1999), Verolme & de Zeeuw (2002) and Cretton & Emsellem (2004) described similar tests using two-integral Schwarzschild models.

5.1 Input two-integral test model

An $f(E, L_z)$ model of NGC 2974 was constructed using the contour integration method of (Hunter & Qian 1993, hereafter HQ); see also Qian et al. (1995). We used the mass model from Section 4.1 parametrized by MGE. This approach follows in detail Emsellem, Dejonghe & Bacon (1999) and, because of the properties of Gaussian functions, simplifies the numerical calculations significantly. Given the density of the system, the HQ method gives the unique even part of the DF, $f_{\rm e} = (1/2)\,[f(E, L_z) + f(E, -L_z)]$ (even in L_z). The odd part can be calculated as a product of the even $f_{\rm e}$ and a prescribed function $h = h(L/L_z)$. The magnitude of the function h is chosen to be smaller than unity, which ensures that the final DF, $f = f_{\rm e} + f_{\rm o}$, is physical (i.e. non-negative, provided that $f_{\rm e} \gg 0$ everywhere). In practice, the odd part is chosen to fit the observed kinematics (mean streaming) by flipping the direction of orbits with respect to the symmetry axis (photometric minor axis).

The two-integral model of NGC 2974 was computed using $i = 60^\circ$ and $\Upsilon = 4.6$. In order to construct a realistic DF, we also included a black hole with mass $M_{\rm BH} = 2.5 \times 10^8\ {\rm M}_\odot$, from the $M_{\rm BH}$–σ relation. The MGE model, constructed from a finite spatial resolution *HST* WFPC2 image, has by construction an unrealistic flat asymptotic density profile well inside the central observed pixel ($r \lesssim 0.02$ arcsec). Therefore, we assumed a cusp with a power-law slope of 1.5 ($\rho = r^{-1.5}$) inside that radius, following the prescription of Emsellem et al. (1999). The final two-integral DF was computed on a fine adaptive grid (i.e. more points in the region of strongly changing DF with $E/E_{\rm max} < 2$, where $E_{\rm max}$ is the value of the central potential of the model excluding the black hole) of 140 × 79 points in (E, L_z). A fine grid of LOSVDs was computed from this DF. These LOSVDs were used to compute the observable LOSVDs on 3721 positions, two-dimensionally covering one quadrant of the sky plane (50 × 50 arcsec^2), accounting for the instrumental set-up (size of SAURON pixels) and atmospheric seeing (which matched the observations of NGC 2974 and was used for the three-integral models in Section 4.2). The parameters of the two-integral model of NGC 2974 are listed in the first column of Table 6.

Table 6. The properties of two-integral models and comparison to three-integral best-fitting results. Column 1 gives the parameters of the two-integral model of NGC 2974. Column 2 gives the recovered parameters using the full field spatial coverage (100 × 100 arcsec^2 effectively) of kinematic constraints. Column 3 gives the recovered parameters using the SAURON field spatial coverage (40 × 40 arcsec^2 effectively) of kinematic constraints.

	$2I$ model (1)	Full field (2)	SAURON field (3)
Υ	4.6	4.6 ± 0.1	4.4 ± 0.1
i	60°	$60^\circ \pm 5^\circ$	$65^\circ \pm 5^\circ$

In order to mimic the real observations (as well as to reduce the number of observables in the fit) we adaptively binned the spatial apertures using the Voronoi tessellation method of Cappellari & Copin (2003) as was done for the observations, assuming Poissonian noise. The final LOSVDs were used to calculate the kinematic moments (V, σ, h_3–h_6) by fitting a Gauss–Hermite series (first row in Fig. 15). These values were adopted as kinematic observables for the three-integral models. From these data we selected two sets of kinematic observables, as follows.

(i) The first set consisted of all 513 spatial bins provided by the two-integral model. In terms of radial coverage this 'full field' set extended somewhat beyond two effective radii for NGC 2974.

(ii) The second set had a limited spatial coverage. It was limited by the extent of the SAURON observations of NGC 2974, approximately covering one effective radius. We call this observational set of 313 bins the 'SAURON field'.

5.2 Recovery of input parameters

Our two-integral models are axisymmetric by construction and all necessary information is given in one quadrant bounded by the symmetry axes (major and minor photometric axes). Hence, the inputs to the three-integral code covered only one quadrant of the galaxy. Although only one quadrant was used for the calculations, we show all maps unfolded for presentation purposes.

The three-integral models were constructed in the same way as described in Section 4.2. For both sets (full field and SAURON field) of kinematic data, we created orbit libraries of $2 \times 41 \times 10 \times 10$ orbits and constructed models on grids of (Υ, i). As for the real data, we used a regularization parameter $\Delta = 4$. The resulting grids are presented in Fig. 14, and the best-fitting models are listed in Table 6. The three-integral models were able to recover the true input parameters within the estimated errors, although the SAURON field models were less accurate.

The kinematic observables computed from the two-integral models are noiseless, without errors or intrinsic scatter typical of real measurements. For each kinematic observable, we assigned a constant error, but representative to the SAURON observations of NGC 2974: 1σ errors for V, σ, h_3 and h_4–h_6 were 4 km s^{-1}, 7 km s^{-1}, 0.03 and 0.04, respectively.

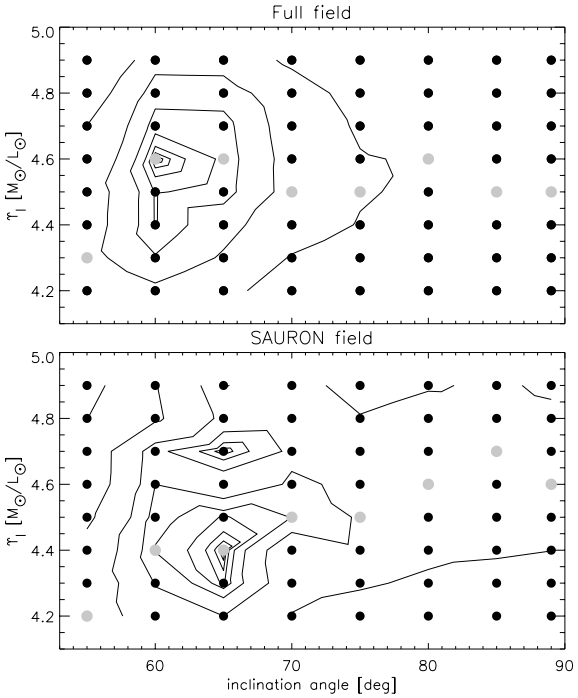

Figure 14. Three-integral model grids of inclination angle versus M/L ratio, Υ. Contours present constant $\Delta\chi^2$, measuring the goodness of fit of the models. Every symbol corresponds to a three-integral axisymmetric model with given inclination angle and Υ. The grey symbols indicate the best-fitting models at a given inclination. The top grid presents models using the full field set of kinematic constraints. The global minimum is for the model with $i = 60^\circ$ and $\Upsilon = 4.6$. The bottom panel presents models using the SAURON field set of kinematic constraints. The global minimum here is for the model with $i = 65^\circ$ and $\Upsilon = 4.4$.

As we wanted to test an ideal situation, we computed the kinematic observables from the two-integral model without adding noise (intrinsic scatter) typical for real measurements. However, given the fact that the input model is noiseless, the χ^2 levels computed from the fit to the kinematics are meaningless. In order to have an estimate of the uncertainties in the recovery of the parameters, we computed half a dozen Monte Carlo realizations of the kinematic data, introducing the intrinsic scatter to the noiseless data. For each Monte Carlo data set, we constructed a three-integral model grid as in Fig. 14. Because of time limitations, we calculated parameter grids (Υ, i) of models with smaller orbit libraries ($2 \times 21 \times 7 \times 7$ orbits) of both full field and SAURON field data sets. In this case we also applied the regularization scheme with $\Delta = 4$. Approximate 3σ confidence levels assigned to the best-fitting parameters are listed in Table 6. Setting the regularization to zero, we observed similar trends.

The numbers in Table 6 suggest that the inclination is formally recovered by three-integral models, as seen in the case of the observation (Section 4.3). We repeated the exercises of plotting a sequence of models with different inclinations (using the full field kinematics). These are presented in Fig. 15 and we can see a very similar trend as in Fig. 12: there appears to be little difference between the models, although by scrutinizing the details, it is possible to choose the best model by eye.

The smoothness of the data of the two-integral test model helps in recognizing the best-fitting model. The models with lower inclination (towards face-on) are generally smoother than the higher inclination (towards edge-on) models, which systematically show radial structures. These 'rays' visible in Fig. 16 are artefacts of the discreteness of our orbit library. The starting points of the orbits correspond to the positions of orbital cusps, which carry the biggest contribution to the observables. The total number of cusps is determined by the number of orbits, and the finiteness of the orbit library is reflected in the discrete contributions of the cusps to the reconstructed observables (see Fig. 1.2 of Cappellari et al. 2004). However, the projection effects increase the smoothness by spatially overlapping different cusps; hence, models projected at, for example, $i = 60^\circ$ will be smoother than models viewed edge on. We believe this effect could influence the χ^2, favouring the lower inclination models.

Although present, this effect does not provide the only constraint on the inclination. When examined more closely, models with low inclination do reproduce certain features better: for example, the shape and amplitude of the velocity dispersion in the central 20 arcsec, h_3 and h_4 at the larger radii (towards the edge of the field), the central 10 arcsec of h_5 and h_6. In all cases, the model with $i = 60^\circ$ reproduces these features better than other models. Comparing the models, the most significant contribution to χ^2 comes from the velocity dispersion; however, generally, individual observables have slightly different χ^2 values, which increase with the inclination moving away from 60° and are visible only as a cumulative effect. This explains the similarities of the different models to the eye, although they are formally significantly different.

The differences in the model observables (which include moments up to h_6) are below the level of the expected systematics in the data (e.g. template mismatch) or in the models (e.g. regularization or variations in the sampling of observables with orbits). In the case of NGC 2974, using high signal-to-noise 2D data, the differences between the models themselves are smaller than between the

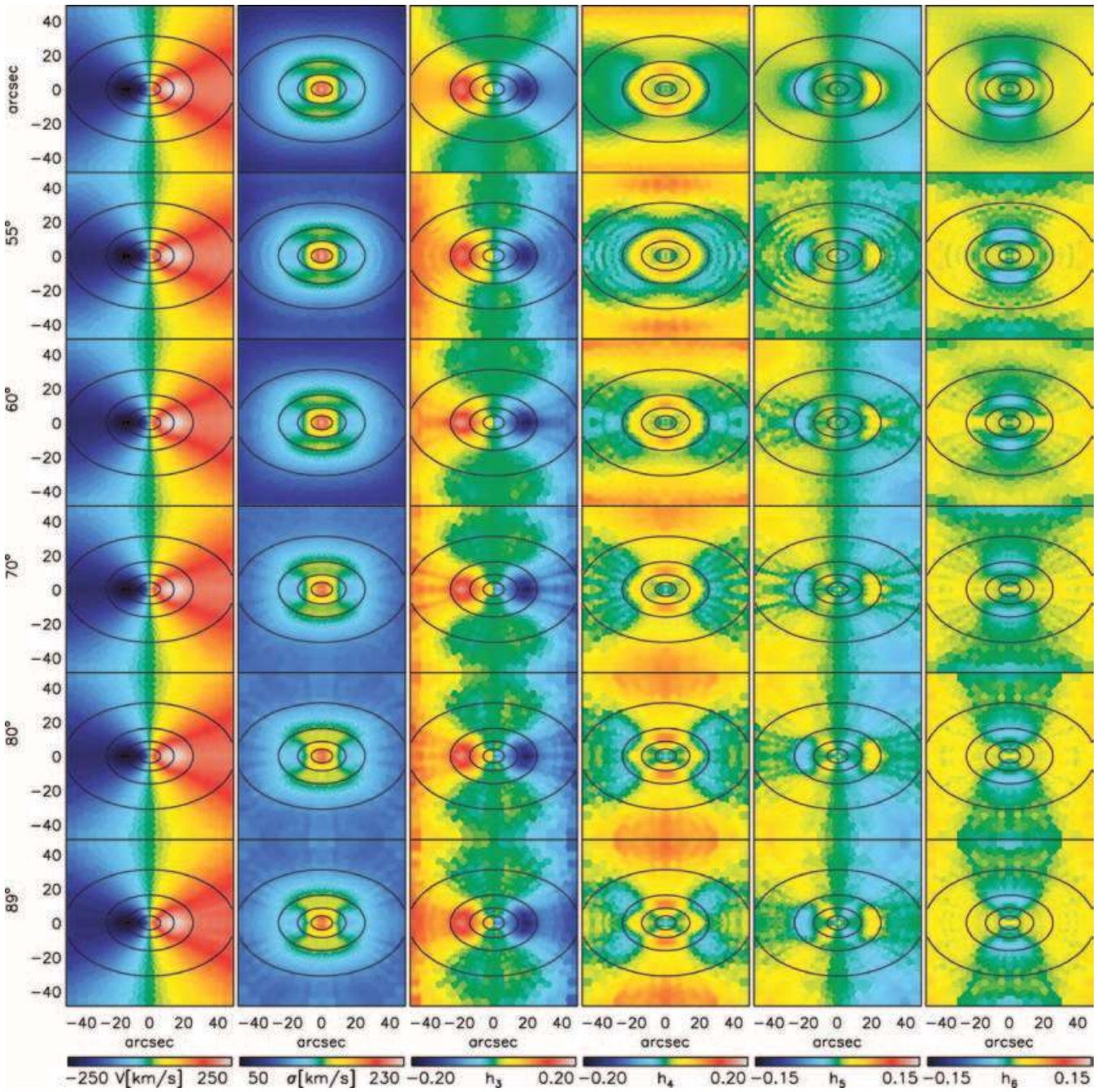

Figure 15. Sequence of three-integral models for different inclinations fitting the full field of kinematic observables. The first row shows the two-integral test model, and subsequent rows show three-integral models for $i = (55^\circ, 60^\circ, 70^\circ, 80^\circ, 89^\circ)$. Columns from left to right present moments of the LOSVD: v, σ and from h_3 to h_6. Isophotal contours of total light are shown with solid lines.

best-fitting model and the data, implying that the inclination is only weakly constrained. This result suggests a fundamental degeneracy for the determination of inclination with three-integral models, which is contrary to indications from previous work by V02. Theoretical work and more general tests on other galaxies are needed for a better understanding of this issue.

5.3 Effect of the field coverage on orbital distribution

The next step is to compare in more detail the three-integral models using the two different kinematic data sets. The kinematic structures of the best-fitting models are presented in Fig. 16. In the region constrained by the kinematic data, both models reproduce equally well the input kinematics. As expected, the regions outside the SAURON field are not reproduced well. It is more interesting to compare the phase spaces of the models. In particular, we wish to see whether the mass weights assigned to the orbits (represented by the integrals of motion) are the same for the two models.

The corresponding integral spaces are shown in Fig. 17. Red rectangular boxes represent the extent of the kinematics used to constrain the models. In the regions constrained by both kinematic sets, the two integral spaces are identical: both models recover the

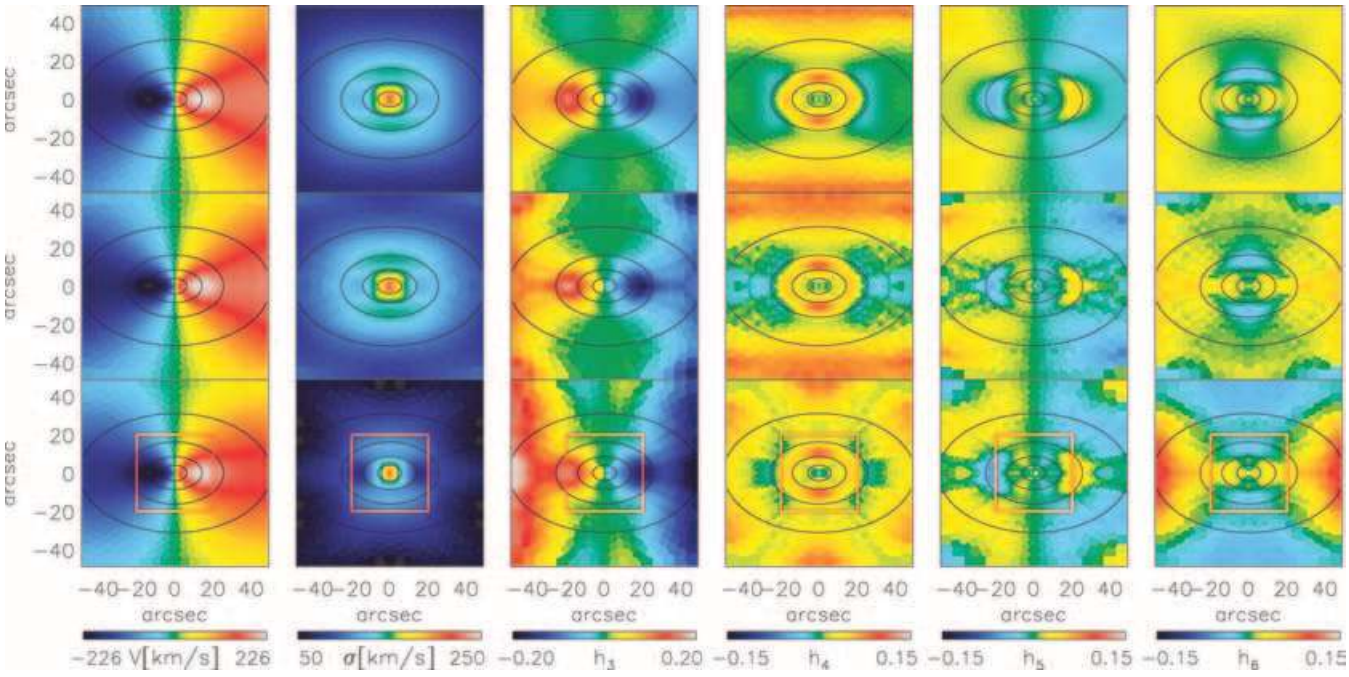

Figure 16. Comparison between two-integral analytical model kinematics and three-integral models. First row: two-integral model used as input to the three-integral code. Second row: best-fitting three-integral model ($i = 60^\circ$, $\Upsilon = 4.6$) using the full field set of kinematic constraints. Third row: best-fitting three-integral model ($i = 65^\circ$, $\Upsilon = 4.4$) using the SAURON field set of kinematics. The spatial extent of this set is marked by red squares on the maps. From left to right, each panel presents mean velocity (V), velocity dispersion (σ) and Gauss–Hermite moments (h_3, h_4, h_5 and h_6). Isophotal contours of total light are shown with solid lines.

indistinguishable orbital mass weights. The differences appear at larger radii (beyond 20 arcsec), outside the area constrained by the SAURON field kinematic set. Putting this result in the perspective of observations, the resulting phase space (in the region constrained by the observations) does not depend on the extent of the radial coverage used to constrain the model. This result strengthens the case of the NGC 2974 modelling results, where we have integral-field observations reaching $\approx 1\, r_e$. The recovered integral space and its features would not change significantly if we had a spatially larger observational field.

5.4 Recovery of the internal moments

We wish to see whether the best-fitting three-integral model to the $f(E, L_z)$ test galaxy model is consistent with the input (i.e. whether three-integral models will recognize the true structure of the test galaxy). A first estimate can be achieved by investigating the internal structure of the resulting model galaxy, specifically the shape of the velocity ellipsoid. We define the tangential dispersion as $\sigma_t = [(1/2)(\sigma_\theta^2 + \sigma_\phi^2)]^{1/2}$. Note that σ_ϕ includes only random motion, so that for an isotropic distribution, under the given definition, the radial (σ_r) and tangential dispersion are equal. Because two-integral models are isotropic in the meridional plane per definition, we expect to recover that σ_r is equal to σ_θ and the cross-term $\sigma_{R\theta}$ is equal to zero. In Fig. 18 we show the ratio of the moments of the velocity ellipsoids at different positions in the meridional plane and at different radii from the model constrained by the full field kinematics. One can see that $\sigma_r = \sigma_\theta$ within $\approx$5 per cent, confirming that our three-integral model recovers the true internal moments. Also, computing the cross-terms $\sigma_{R\theta}$, we verified that it is negligible everywhere. Similar results are also recovered from the SAURON field model: in the constrained region the ratio of σ_r and σ_θ moments is consistent with unity.

5.5 Recovery of the distribution function

The previous result shows that the constructed three-integral model is a consistent representation of the input $f(E, L_z)$ model. However, a more conclusive test is to compare the DFs.

The results of the three-integral Schwarzschild method are orbital mass weights, $\gamma'_{3I}(E, L_z, I_3)$, for each set of integrals of motion (E, L_z, I_3), which define an orbit. The DF is related to the mass weights via the phase-space volume (for a detailed treatment, see Vandervoort 1984)

$$\gamma(E, L_z, I_3)\,\mathrm{d}E\,\mathrm{d}L_z\,\mathrm{d}I_3 = f(E, L_z, I_3) \times \Delta V(E, L_z, I_3)\,\mathrm{d}E\,\mathrm{d}L_z\,\mathrm{d}I_3, \tag{6}$$

where

$$\Delta V(E, L_z, I_3) = \int_\Omega \mathcal{J}(\boldsymbol{x}, E, L_z, I_3)\,\mathrm{d}^3x, \tag{7}$$

and $\mathcal{J}(\boldsymbol{x}, E, L_z, I_3)$ is the Jacobian of the coordinate transformation from $(\boldsymbol{x}, \boldsymbol{v})$ to $(\boldsymbol{x}, E, L_z, I_3)$, and Ω is the configuration space accessible to an orbit defined by the integrals (E, L_z, I_3). Unfortunately, I_3 is not known analytically, so the above relation cannot be explicitly evaluated, except for separable models. For this reason we limit ourselves to test the consistency of our three-integral mass weights with the input two-integral DF. This is possible, because if the recovered three-integral DF is equal to the input DF, then the mass $\gamma_{2I}(E, L_z)$ assigned to the stars in a given range of (E, L_z) by the three-integral model has to be equal to the mass in the same range of the input model.

There exists a precise relation between the input two-integral DF, $f = f(E, L_z)$, and the corresponding orbital mass weights, $\gamma_{2I}(E, Lz)$. The total mass of the system is the integral of the DF over the phase-space. Using this, Cretton et al. (1999) derived the expression

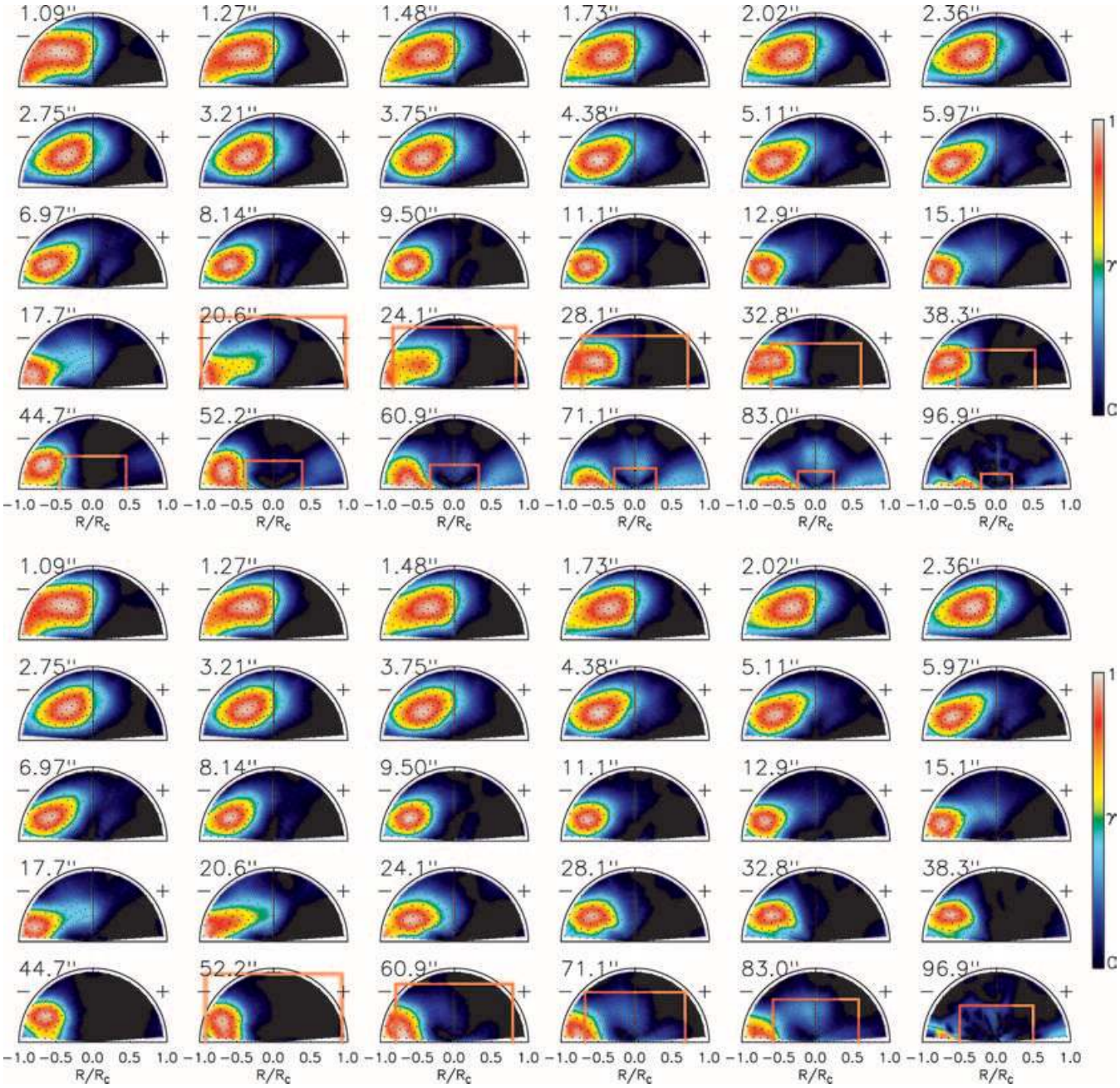

Figure 17. Comparison of the integral spaces of the $f(E, L_z)$ test models. The upper five rows belong to the model constrained by the SAURON field kinematics and the lower five rows to the model constrained by the full field kinematics. The meaning of each panel is the same as in Fig. 13. The colour bar on the right represents the relative colour coding of the orbital mass weights (γ), where 1 represents the largest mass weight assigned to an orbit at the given energy. In the region constrained by both kinematic sets, the integral spaces are indistinguishable.

for the mass weights in appendix B of their paper (equation B4)

$$\gamma_{2I}(E, L_z) = \int_{\Omega} \frac{\mathrm{d}M}{\mathrm{d}E\mathrm{d}L_z}\mathrm{d}E\,\mathrm{d}L_z \tag{8}$$

with

$$\frac{\mathrm{d}M}{\mathrm{d}E\mathrm{d}L_z} = f(E, L_z) \oint_{ZVC(E,L_z)} (R\,\mathrm{d}z - z\,\mathrm{d}R) \tag{9}$$

where the contour integral yields the area of the zero velocity curve (ZVC). Before applying equations (8) and (9) on the two-integral DF, we rebinned it to the same grid of ΔE and ΔL_z as the three-integral mass weights. Finally, we approximate the integral (8) by multiplying the mass fraction in each grid cell by $\Delta E \Delta L_z$.

For our comparison we defined as the energy intervals the set of energies used in the construction of the three-integral models (total of 41). The interval in angular momentum was defined as a step of 0.1 of $L_z/L_z^{\max}$ from -1 to $+1$ (total of 20) for a given energy. The resulting grid of orbital weights is relatively coarse, but is representative of the model. The agreement between the two sets of mass weights is shown in Fig. 19 . The main features of the given two-integral test model are well reproduced by the

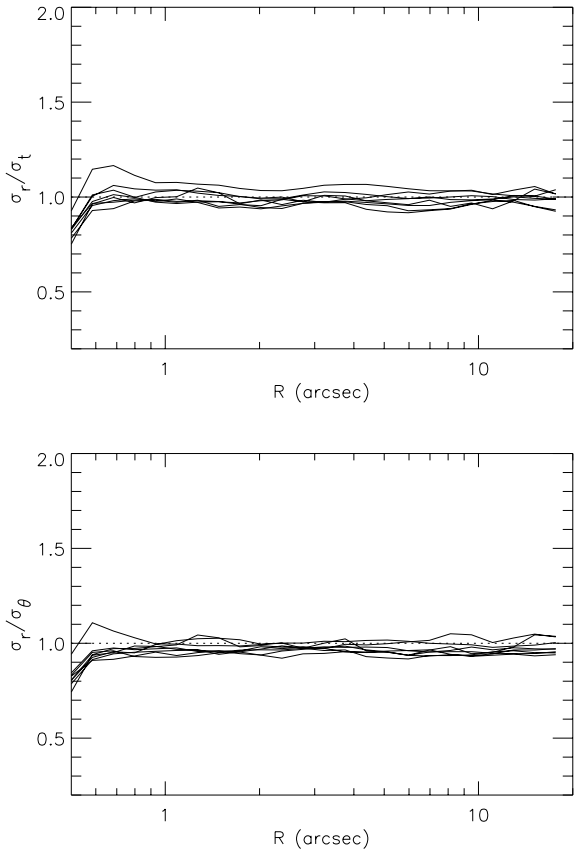

Figure 18. Moments of the velocity ellipsoid for the two-integral test galaxy recovered by the three-integral model (constrained by the full field kinematic set). The upper panel shows the ratio of the radial and tangential moment as defined in the text. The lower panel presents the ratio of the radial and latitudinal moments. Different lines show the ratio of the moments in the meridional plane at different PAs, starting from the major axis to the minor axis. In a true two-integral galaxy, all three moments of the velocity ellipsoid have to be equal. Note that the deviation inside 1 arcsec is expected because the data do not constrain the model in that region.

three-integral model. Again, the mass weights should be compared in the region constrained by the data (between the vertical lines in the figure). In order to quantify the agreement, we restricted the comparison to the part of the distribution of mass weights contributing significantly to the model inside this region, roughly bounded by the green levels in Fig. 19. This selected region contains about 97 per cent of mass. The mean absolute deviation between the two sets of mass weights is 6 per cent, with peaks around 15 per cent, except for a narrow region towards the edge of the kinematic coverage around $E = -8 \times 10^4$ km^2 s^{-2} and with $L_z/L_{\rm Lz}^{\rm max} > 0$, where deviations can reach 35 per cent. The mass weights of the three-integral model are also relatively noisy, which is mostly the consequence of imposed discreteness as well as the numerical nature of the method.

From our test model, where the potential is known, we conclude that the Schwarzschild method can reliably recover the input DF within the region constrained by 2D kinematics (including higher-order moments). We have already shown that the existence of constraints outside an effective radius does not significantly affect the orbital distribution inside an effective radius. This suggests that, in the region constrained by integral-field kinematics, a representative DF can be recovered using the Schwarzschild method.

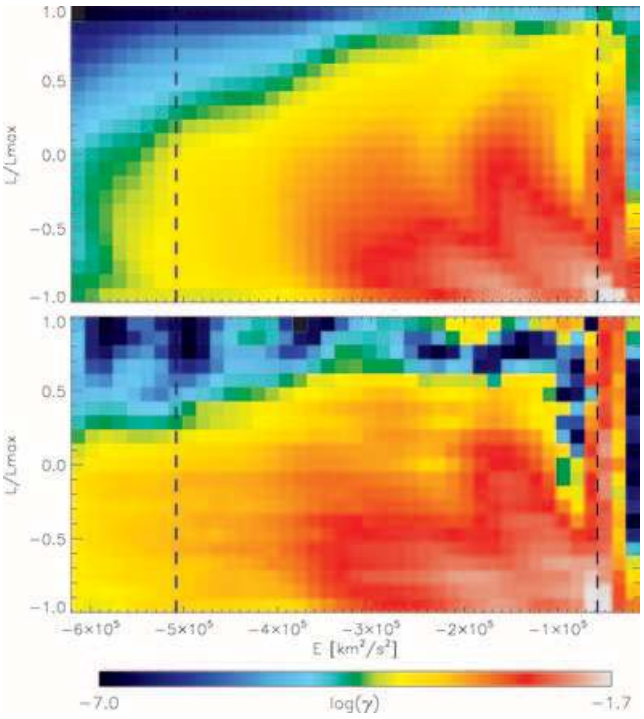

Figure 19. Comparison of the mass weights from the two-integral model (upper panel) and the results of the three-integral modelling (lower panel) using the two-integral model as input. The galaxy centre is on the left side. The first bin containing the contribution of the black hole was not plotted, because the resolution of the models does not allow for its recovery. The two vertical lines enclose the region constrained by the kinematic data. The colour bar represents the colour coding of the orbital mass weights (γ) in log scale assigned to any interval of (E, L_z). There are two main differences between the input and the best-fitting model: (i) the horizontal stripes, which are a result of the discrete way in which we select orbits in L_z range; (ii) the mass weights at high L_z values, which, however, contain a very small fraction of the galaxy mass and are not significant.

6 MODELLING OF EMISSION-LINE GAS

Clearly, with its prominent gas component, NGC 2974 is an unusual elliptical galaxy. The observations indicate the morphological similarity between the small-scale (H II) and large-scale (H I) gas discs. Also, long-slit measurements of stellar and gas motions detect similarities between the stellar and gas kinematics (Kim 1989; Cinzano & van der Marel 1994). In this section we investigate the inclination of the gaseous component as well as constructing a dynamical Jeans model of the gas disc, as in Cinzano & van der Marel (1994), in order to compare them to the results of the stellar dynamical modelling.

6.1 Inclination of the gas disc

The existence of the emission-line gas disc in NGC 2974 can be used to infer the inclination of the galaxy assuming an equilibrium dynamical configuration. This has been attempted before, and in all studies the inclination of the gas disc was consistent with 55°–60°: 55° (Amico et al. 1993); 59° (Buson et al. 1993); 57.°5 (Cinzano & van der Marel 1994); 60° (Plana et al. 1998). The high quality of the 2D SAURON kinematics allows us to estimate the inclination of the emission-line gas disc more accurately.

We assume the motion of the emission-line gas is confined to a thin axisymmetric disc. We neglect the deviations from axisymmetry discussed in Section 3, and symmetrize the gas velocity map in the

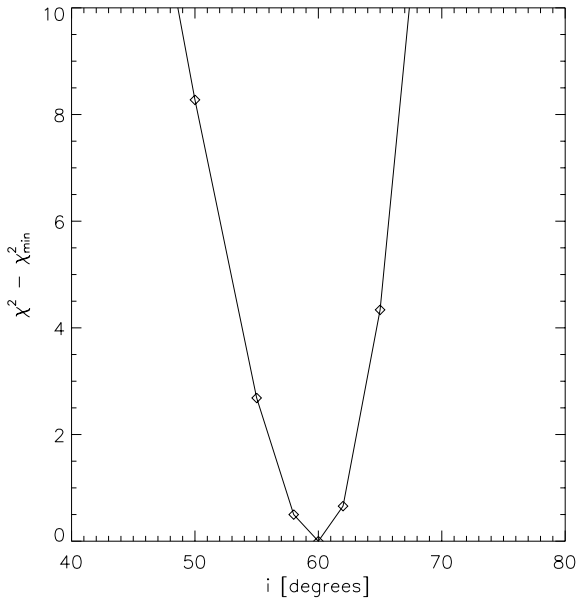

Figure 20. $\Delta\chi^2$ as a function of inclination obtained by comparing the symmetrized data for NGC 2974 and the model gas disc velocity map described in Section 6.1.

same way as the stellar velocity map in Section 4.3. This velocity map is an axisymmetric representation of the observed field, which can be compared to an axisymmetric model of the disc velocity maps. Constructing a model axisymmetric 2D velocity map requires only the kinematic major axis velocity profile v'_{mj}. The entire map is then given by the standard projection formula

$$v_{\rm LOS}(x', y') = v_\phi \left(\frac{x' \sin i}{r}\right) = v'_{mj}\left(\frac{x'}{r}\right), \qquad (10)$$

where $r^2 = x'^2 + (y'/\cos\ i)^2$ and i is the inclination of the disc. It is clear from this formula that for a given observed major-axis velocity, the velocity field is just a function of inclination. From the first three odd coefficients (c_1, c_3 and c_5) of the kinemetric expansion, we constructed the velocity profile v'_{mj} along the major axis ($\theta = \overline{\phi_1}$). Using the major axis velocity profile, we created a set of disc velocity fields inclined at different values of i, and compared them with the symmetrized velocity field. We did not correct for the influence of the PSF, as this effect is small and is confined to the central few arcsec, which we excluded from the comparison. We also compared the models with the non-symmetrized velocity map and the results were in very good agreement, but with a slightly larger uncertainty range.

Fig. 20 presents the $\Delta\chi^2$ obtained by subtracting the disc model velocity field from the symmetrized measurements. The best-fitting inclination is $i = 60^\circ \pm 3^\circ$ (at 1σ level). Fig. 21 shows a comparison between the symmetrized and model velocity fields for a few representative inclinations. The differences between the model fields are mostly in the opening angle of the iso-velocity contours, which change with the inclination of the field. The opening angle of the model with $i = 60^\circ$ is the most similar to the observed velocity field, and this significantly lowers the χ^2 of the fit.

The best-fitting inclination of 60° for the emission-line gas is in excellent agreement with literature values determined from the various gas components. Our best-fitting three-integral stellar dynamical model was obtained for an inclination of 65° with 3σ uncertainty of 2°.5. This inclination is close to the inclination of 60° presented in this section, suggesting a good agreement between the stellar and gaseous models. However, there is the concern that the agreement may not be as significant as it seems in light of the tests and results from Section 5.2.

6.2 Simple dynamical model for the disc

At large scale, the gas kinematic maps are consistent with the assumption that the emission-line gas is moving in a thin disc. This assumption clearly breaks down in the inner few arcsec, but at this point we neglect this effect. The observed gas velocity dispersion is high everywhere in the disc and is much larger than the thermal velocity dispersion, which should be of the order of $\sigma_{\rm thermal} \sim 10$ km s^{-1} (Osterbrock 1989) and in any case <30 km s^{-1}. Clearly, in addition to the thermal dispersion, the gas has another source of motion, which is not presently understood, but is seen in many galaxies (Bertola et al. 1995). Several studies (e.g. van der Marel & van den Bosch 1998; Verdoes Kleijn et al. 2000) have assumed that the non-thermal gas velocity dispersion is the result of 'local turbulence', without describing the details of the underlying physical processes. In this assumption, the gas still rotates at the circular velocity and the invoked turbulence does not disturb the bulk flow of the gas on circular orbits. The alternative to this assumption is that the non-thermal velocity dispersion component comes from collisionless gravitational motion of the gas, where the gas acts like stars: clumps of gas move on self-intersecting orbits. This is, perhaps, not very physical for gas in general, but it can be applied to estimate the difference between the circular and streaming velocity (and including the projection effect on the observed velocity) of the gas. Several studies have used this approach successfully (e.g. Cinzano & van der Marel 1994; Cretton, Rix & de Zeeuw 2000; Barth et al. 2001; Aguerri, Debattista & Corsini 2003; Debattista & Williams 2004). Presently, the role and importance of the asymmetric drift remains an unresolved issue.

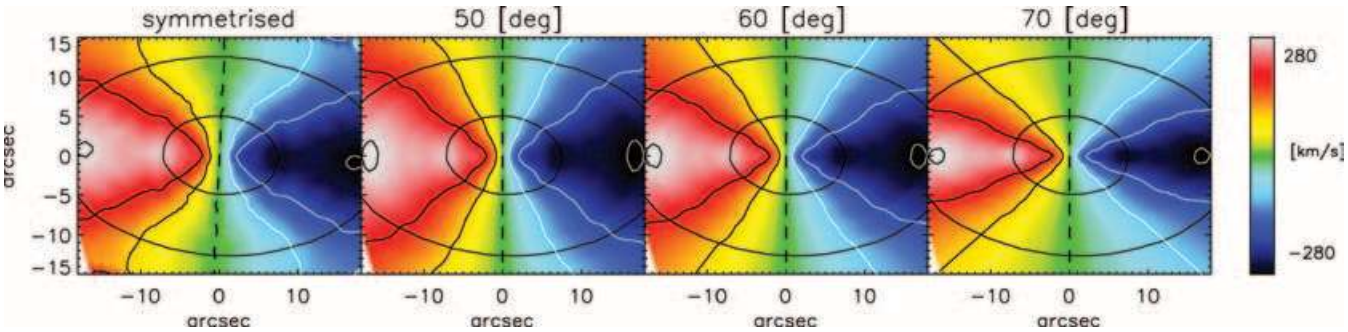

Figure 21. Comparisons between observed and model gas disc velocity fields. From left to right: observations (symmetrized), model maps for inclinations of 50°, 60° (best-fitting), 70°. Isophotal contours of total light are presented with ellipses.

In constructing our simple disc model, we have assumed that the emission-line gas is moving in individual clumps that interact only collisionlessly. The clumps move along ballistic trajectories in a thin disc, under the influence of the galaxy potential given by the stellar distribution (Section 4). The gas kinematics are determined by solving the Jeans equations for radial hydrostatic equilibrium. Following (Binney & Tremaine 1987, equation 4-33), the streaming velocity of gas can be written in cylindrical coordinates as

$$\bar{v}_\phi^2 = V_c^2 - \sigma_R^2 \left[-R\frac{\mathrm{d}\ln\rho}{\mathrm{d}R} - R\frac{\mathrm{d}\ln\sigma_R^2}{\mathrm{d}R} - \left(1 - \frac{\sigma_\phi^2}{\sigma_R^2}\right)\right] \qquad (11)$$

where we have assumed that the DF depends on the two classical integrals of motion: $f = f(E, L_z)$, which implies $\sigma_R = \sigma_z$ and $\overline{v_R v_z} = 0$. In equation (11), V_c is the circular velocity $[\sqrt{R(\mathrm{d}\Phi/\mathrm{d}R)}]$, Φ is the total potential of the galaxy obtained from the MGE fit assuming inclination i, σ_R and σ_ϕ are the radial and azimuthal velocity dispersions, and $\rho(R)$ is the spatial number density of gas clouds in the disc. Lacking any alternative, we use the surface brightness of the gas to estimate $\rho(R)$. Instead of using the actual measured values of the [O III] and Hβ flux, we parametrize the emission-line surface brightness with a double exponential law

$$\rho = \rho_0 \exp\left(-\frac{R}{R_0}\right) + \rho_1 \exp\left(-\frac{R}{R_1}\right), \qquad (12)$$

in order to decrease the noise. The parameters are obtained from the fit to the [O III] data shown in (Fig. 22), where the 2D surface brightness was collapsed to a profile by averaging along ellipses of constant ellipticity (ellipticity of the galaxy) and position angle (PA of the galaxy). The errors are standard deviations of the measurements along each ellipse.

The relation between radial and azimuthal velocity dispersions can be obtained using the epicyclic approximation. This gives (following equation 4-52 in Binney & Tremaine 1987)

$$\frac{\sigma_\phi^2}{\sigma_R^2} = \frac{1}{2}\left(1 + \frac{\mathrm{d}\ln V_c}{\mathrm{d}\ln R}\right). \qquad (13)$$

This approximation is valid for small values of the asymmetric drift $v_\phi - V_c$, or, in other words, in the limit of a cold disc with small velocity dispersion, $\sigma \ll V_c$. This is marginally the case in NGC 2974, clearly violated in the central <5 arcsec, but it is acceptable in most of the observed regions (Fig. 23).

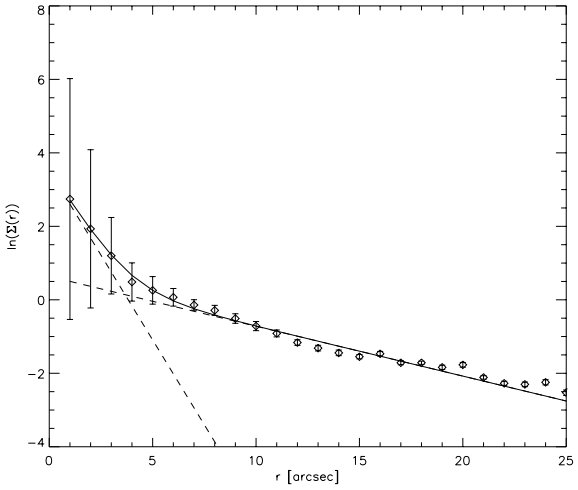

Figure 22. Fit to the surface-density profile of the [O III] emission lines. Dashed lines present individual exponentials given by equation (12).

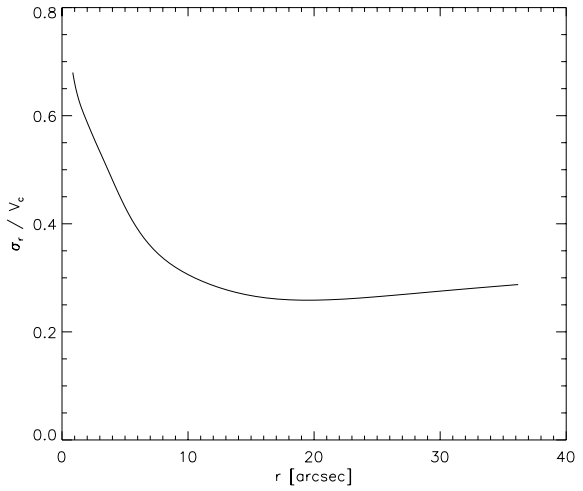

Figure 23. Ratio σ_R/V_c for the best-fitting model to the emission-line gas data.

The observed quantities can be obtained from the calculated intrinsic properties projecting at an inclination angle i. The projected 2D LOS velocity field is given by equation (10). Within these assumptions of the disc model, the projected LOS velocity dispersion is

$$\sigma_{\mathrm{LOS}}^2 = \left(\sigma_\phi^2 - \sigma_R^2\right)\left(\frac{x' \sin i}{r}\right)^2 + \sigma_R^2. \qquad (14)$$

We constructed the asymmetric drift models of the emission-line gas in NGC 2974 using the MGE parametrization of the potential, $\Upsilon = 4.5$, inclination $i = 60^\circ$, and simultaneously accounting for the atmospheric seeing and pixel size of the SAURON observations (see Qian et al. 1995 for details). In the process we assumed an exponential law for the radial velocity dispersion

$$\sigma_R = \sigma_0 + \sigma_1 \exp\left(-\frac{R}{R_\sigma}\right). \qquad (15)$$

Our models therefore have three free parameters (σ_0, σ_1 and R_σ), and varying them we constructed gaseous disc models of NGC 2974. The models were compared with the symmetrized velocity and velocity dispersion maps averaging the four symmetric positions on the maps as required for an axisymmetric map (Section 4.3). The best-fitting model was obtained for $\sigma_0 = 85 \pm 5$ km s^{-1}, $\sigma_1 = 180 \pm 10$ km s^{-1} and $R_\sigma = 5 \pm 1$ arcsec. A comparison of this model with the symmetrized observations is presented in Fig. 24.

This simple asymmetric drift model can reproduce rather well the general properties of the emission-line gas disc, including the bulk of the streaming velocity as well as the significant non-zero velocity dispersion. The overall fit is quite good, with a mean difference of only 5 per cent, with peaks up to about 20 per cent. The main discrepancy occurs along the major axis at a radius around 10 arcsec, close to where we observe the presumed elliptical ring in the ionized gas equivalent width (see Fig. 6). The observed minor-axis elongation of the gas velocity dispersion is also not reproduced by the model. This is not surprising because some of those features, as mentioned, are signatures of non-axisymmetry in NGC 2974, and cannot be represented by simple axisymmetric models.

Because the normalization of the kinematics is mostly controlled by the assumed mass-to-light ratio, the goodness of the fit implies that the overall energy budget coming from the Schwarzschild modelling is consistent with the observed gas kinematics; the high value

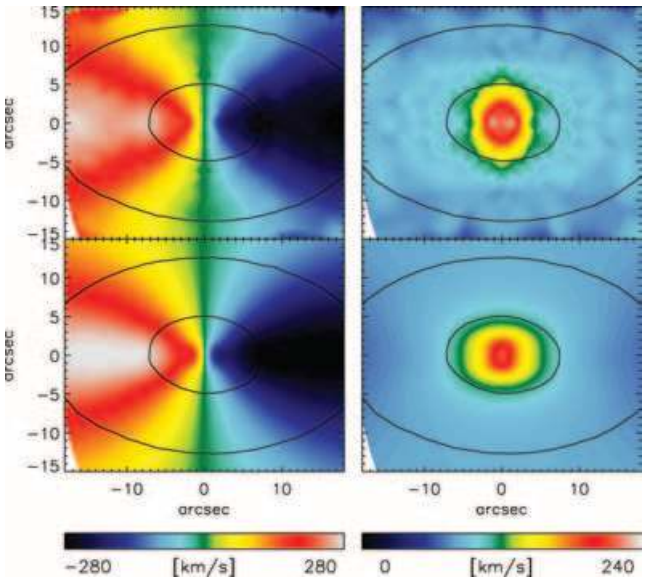

Figure 24. The lower panels show the asymmetric drift model for the best-fitting parameters compared to the top panels, which show the symmetrized (mirror-(anti)symmetric filtering with six terms) mean velocity (first column) and velocity dispersion (second column). Overplotted isophotes are levels of the reconstructed total intensity.

of the gas velocity dispersion is therefore globally compensated by a lower mean velocity. A similar finding was reported by Cinzano & van der Marel (1994). All this therefore raises the question of how the gas can remain dynamically hot in a disc galaxy such as NGC 2974 at a scale of ∼1 kpc.

7 CONCLUDING REMARKS

In this paper we have presented a case study of the early-type galaxy NGC 2974, which was observed in the course of the SAURON survey of nearby E/S0 galaxies.

Kinematic PAs of the stellar and gaseous kinematics of this galaxy are on average well aligned. The stellar kinematic maps exhibit point-(anti)symmetry and mirror-(anti)symmetry, with the kinematic angle equal to the photometric PA, and are consistent with an axisymmetric intrinsic shape. The gaseous velocity map is more complicated, with clear departures from axisymmetry in the centre of the galaxy (<4 arcsec). At larger radii, the gas kinematic angle is not constant, although is largely consistent with the photometric PA, showing deviations of a few degrees. The SAURON observations of NGC 2974 confirm the existence of non-axisymmetric perturbations consistent with an inner bar (EGF03) as well as a possible large-scale bar. The departures from axisymmetry are not visible in the stellar kinematic maps and therefore are likely to be weak. This allows us to construct axisymmetric models of NGC 2974.

We constructed self-consistent three-integral axisymmetric models based on the Schwarzschild orbit-superposition method, varying mass-to-light ratio and inclination. The observed surface brightness was parametrized by the MGE model on both ground- and space-based imaging. The models were compared with the SAURON kinematic maps of the first six moments of the LOSVD (v, σ and h_3–h_6). The best-fitting model has $\Upsilon = 4.5 \pm 0.1$ and $i = 65^\circ \pm 2.^\circ 5$. The inclination is formally well constrained, but there are several indications that the recovery of the inclination is uncertain: (i) differences between the models are on the level of the expected systematics in the data (e.g. template mismatch); (ii) differences between the best-fitting model and the data are bigger than differences between other models and the best-fitting model; (iii) limitations of the models (discreteness of the cusps) may artificially constrain the inclination.

The internal structure of NGC 2974 (assuming axisymmetry) reveals the existence of a rapidly rotating component contributing with about 10 per cent of the total light. This component is composed of orbits allowing the third integral and does not represent a cold stellar disc, although it suggests a flattened structure similar to an S0 galaxy.

The results of the stellar dynamical models were compared with the results of modelling the gas component. The inclination of the gas disc, calculated from the emission-line velocity map, is $i = 60^\circ \pm 3$, in agreement with the formally constrained stellar inclination. A simple model of the gas disc in the same potential used for the stellar modelling ($\Upsilon = 4.5$, but $i = 60^\circ$) was able to reproduce the characteristics of the gas kinematics (v and σ) on a large scale, but, as expected, failed in the centre. In general, the observed gas kinematics is consistent with being produced by the gravitational potential determined by the stellar dynamical models, but the origin of the high-velocity dispersion of the gas on large scales remains an open question.

We performed a set of tests of our implementation of the Schwarzschild orbit-superposition method. For this purpose we constructed a general two-integral model of NGC 2974, and used the reconstructed kinematics as inputs to the Schwarzschild method. We tested (i) the influence of the radial coverage of the kinematic data on the internal structure, (ii) the recovery of the test model parameters (Υ, i) and (iii) the recovery of the test model DF. The tests show the following.

(i) Increasing the radial coverage of the kinematic data from $1r_e$ to $2r_e$ does not change the internal structure within $1r_e$. The results of the dynamical models of the SAURON observations of NGC 2974 would not change if the radial coverage would be increased by a factor of 2.

(ii) We find that three-integral models can accurately recover the mass-to-light ratio. Although the models are also able to constrain the inclination of the test model formally, the apparent differences between the models are small (as in the case of the real observations). Under careful examination, it is possible to choose the best model by eye, but the decisive kinematic features are below (or at the level) of the expected systematics in the data (e.g. template mismatch) and might be influenced by the uncertainties in the models (e.g. regularization or variations in the sampling of observables with orbits). This suggests a degeneracy of models with respect to the recovery of inclination. More general tests on other galaxies and theoretical work are needed for a better understanding of this issue.

(iii) From a realistic test model, the analytically known input DF is recovered within 6 per cent in the region constrained by integral-field kinematics. This suggests that applying the Schwarzschild technique with integral-field kinematics can reliably recover a representative DF.

ACKNOWLEDGMENTS

We thank Glenn van de Ven for fruitful discussions about the recovery of the DF. DK was supported by NOVA, the Netherlands Research school for Astronomy. MC acknowledges support from a VENI grant award by the Netherlands Organization of Scientific Research (NWO).

REFERENCES

Aguerri J. A. L., Debattista V. P., Corsini E. M., 2003, MNRAS, 338, 465
Amico P. et al., 1993, in Danziger I. J., Zellinger W. W., Kjaerp K., eds, Structure, Dynamics and Chemical Evolution of Elliptical Galaxies. ESO, Garching, p. 225
Bacon R. et al., 2001, MNRAS, 326, 23
Barth A. J., Sarzi M., Rix H., Ho L. C., Filippenko A. V., Sargent W. L. W., 2001, ApJ, 555, 685
Bender R., 1988, A&A, 193, L7
Bertola F., Cinzano P., Corsini E. M., Rix H., Zeilinger W. W., 1995, ApJ, 448, L13
Binney J., Tremaine S., 1987, Galactic Dynamics. Princeton Univ. Press Princeton
Bregman J. N., Hogg D. E., Roberts M. S., 1992, ApJ, 387, 484
Buson L. M. et al., 1993, A&A, 280, 409
Cappellari M., 2002, MNRAS, 333, 400
Cappellari M., Copin Y., 2003, MNRAS, 342, 345
Cappellari M., Emsellem E., 2004, PASP, 116, 138
Cappellari M., Verolme E. K., van der Marel R. P., Kleijn G. A. V., Illingworth G. D., Franx M., Carollo C. M., de Zeeuw P. T., 2002, ApJ, 578, 787 (C02)
Cappellari M. et al., 2004, in Ho L.C., ed., Carnegie Observatories Astrophysics Series, Vol. 1, Coevolution of Black Holes and Galaxies. Carnegie Observatories, Pasadena (http://www.ociw.edu/ociw/symposia/series/symposium1/proceedings.html)
Cinzano P., van der Marel R. P., 1994, MNRAS, 270, 325
Copin Y. et al., 2001, in Combes F., Barret D., Thévenin F., eds, SF2A-2001: Semaine de l'Astrophysique Francaise. Kinemetry: quantifying kinematic maps. EdP Sciences, Les Ulis, France, p. 289
Copin Y., Cretton N., Emsellem E., 2004, A&A, 415, 889
Cretton N., Emsellem E., 2004, MNRAS, 347, L31
Cretton N., van den Bosch F. C., 1999, ApJ, 514, 704
Cretton N., de Zeeuw P. T., van der Marel R. P., Rix H., 1999, ApJS, 124, 383
Cretton N., Rix H., de Zeeuw P. T., 2000, ApJ, 536, 319
de Zeeuw P. T. et al., 2002, MNRAS, 329, 513
Debattista V. P., Williams T. B., 2004, ApJ, 605, 714
Emsellem E., Monnet G., Bacon R., 1994, A&A, 285, 723
Emsellem E., Dejonghe H., Bacon R., 1999, MNRAS, 303, 495
Emsellem E., Goudfrooij P., Ferruit P., 2003, MNRAS, 345, 1297 (EGF03)
Emsellem E. et al., 2004, MNRAS, 352, 721 (E04)
Erwin P., Sparke L. S., 2002, AJ, 124, 65
Erwin P., Sparke L. S., 2003, ApJS, 146, 299
Franx M., van Gorkom J. H., de Zeeuw T., 1994, ApJ, 436, 642
Friedli D., Martinet L., 1993, A&A, 277, 27
Gebhardt K. et al., 2003, ApJ, 583, 92
Gerhard O. E., 1993, MNRAS, 265, 213
Goudfrooij P., Hansen L., Jorgensen H. E., Norgaard-Nielsen H. U., de Jong T., van den Hoek L. B., 1994, A&AS, 104, 179
Hunter C., Qian E., 1993, MNRAS, 262, 401 (HQ)
Kim D., 1989, ApJ, 346, 653
Kim D.-W., Jura M., Guhathakurta P., Knapp G. R., van Gorkom J. H., 1988, ApJ, 330, 684
Kirst J., Hook R., 2001, The Tiny Tim User's Manual version 6.0
Laine S., Shlosman I., Knapen J. H., Peletier R. F., 2002, ApJ, 567, 97
Lawson C. L., Hanson R. J., 1974, Solving Least-Squares Problems, Prentice-Hall Series in Automatic Computation. Prentice-Hall, Englewood Cliffs, NJ
Osterbrock D. E., 1989, Astrophysics of Gaseous Nebulae and Active Galactic Nuclei. University Science Books, Sausalito, CA
Pfenniger D., Norman C., 1990, ApJ, 363, 391
Plana H., Boulesteix J., Amram P., Carignan C., Mendes de Oliveira C., 1998, A&AS, 128, 75
Press W. H., Teukolsky S. A., Vetterling W. T., Flannery B. P., 1992, Numerical Recipes in FORTRAN 77, 2nd edn. Cambridge Univ. Press, Cambridge
Qian E. E., de Zeeuw P. T., van der Marel R. P., Hunter C., 1995, MNRAS, 274, 602
Rix H., White S. D. M., 1992, MNRAS, 254, 389
Rix H., de Zeeuw P. T., Cretton N., van der Marel R. P., Carollo C. M., 1997, ApJ, 488, 702
Rybicki G. B., 1987, in de Zeeuw P. T., ed., Proc. IAU Symp. 127, Structure and Dynamics of Elliptical Galaxies. Reidel, Dordrecht, p. 397
Schoenmakers R. H. M., Franx M., de Zeeuw P. T., 1997, MNRAS, 292, 349
Schwarzschild M., 1979, ApJ, 232, 236
Schwarzschild M., 1982, ApJ, 263, 599
Thomas J., Saglia R. P., Bender R., Thomas D., Gebhardt K., Magorrian J., Richstone D., 2004, MNRAS, 353, 391
Tonry J. L., Dressler A., Blakeslee J. P., Ajhar E. A., Fletcher A. B., Luppino G. A., Metzger M. R., Moore C. B., 2001, ApJ, 546, 681
Tremaine S. et al., 2002, ApJ, 574, 740
Valluri M., Merritt D., Emsellem E., 2004, ApJ, 602, 66
van der Marel R. P., Franx M., 1993, ApJ, 407, 525
van der Marel R. P., van den Bosch F. C., 1998, AJ, 116, 2220
van der Marel R. P., Cretton N., de Zeeuw P. T., Rix H., 1998, ApJ, 493, 613
Vandervoort P. O., 1984, ApJ, 287, 475
Verdoes Kleijn G. A., van der Marel R. P., Carollo C. M., de Zeeuw P. T., 2000, AJ, 120, 1221
Verolme E. K., de Zeeuw P. T., 2002, MNRAS, 331, 959
Verolme E. K. et al., 2002, MNRAS, 335, 517 (V02)
Wong T., Blitz L., Bosma A., 2004, ApJ, 605, 183

This paper has been typeset from a TEX/LATEX file prepared by the author.